

Probabilistic Precipitation Nowcasting with Rectified Flow Transformers

Johannes Schusterbauer* Jannik Wiese* Nick Stracke Timy Phan Björn Ommer

CompVis @ LMU Munich Munich Center for Machine Learning (MCML)

Abstract

Accurate weather forecasts are essential across various domains and are safety-critical in extreme weather conditions. Compared to simulation-based forecasting, data-driven approaches show greater efficiency, enabling short-term, high-resolution nowcasting. In particular, diffusion models proved effective in weather nowcasting due to their strong probabilistic foundation. However, existing methods rely on deterministic compression to reduce the complexity of high-dimensional weather data, limiting their ability to capture uncertainty in the decoding process. In this work, we introduce *FREUD*, a **F**rame-wise **E**ncoder and **U**nited **D**ecoder model based on rectified flow transformers for efficient compression of spatio-temporal weather data. Frame-wise encoding enables continuous forecast updates, while the unified video decoder ensures temporal consistency. Our uncertainty-preserving first stage allows us to capture aleatoric uncertainty via ensembling, which is particularly beneficial for extreme weather events with high decoding variability. We achieve state-of-the-art performance in precipitation nowcasting with a compact latent-space rectified flow transformer on the *SEVIR* benchmark and show further performance gains by model and test-time scaling. Code available here: <https://github.com/CompVis/weather-rf>.

1. Introduction

Accurate weather forecasting underpins many industries, including energy production [128, 141, 148], agriculture [23, 105, 116], and aviation [30, 95, 106] and is safety-critical during extreme weather events. Nowcasting refers to short-term, high-resolution forecasts over 30 minutes to 12 hours [31, 33, 136] and requires rapid updates, rendering slow numerical weather prediction models less useful. Data-driven machine learning (ML) models overcome this speed bottleneck [1, 136], but deterministic formulations often blur predictions by averaging over multiple plausible futures [31, 33, 136]. Sampling from probabilistic generative models yields sharp, diverse forecasts, whose spread naturally captures predictive uncertainty [14, 37, 71, 107, 122].

*Equal Contribution.

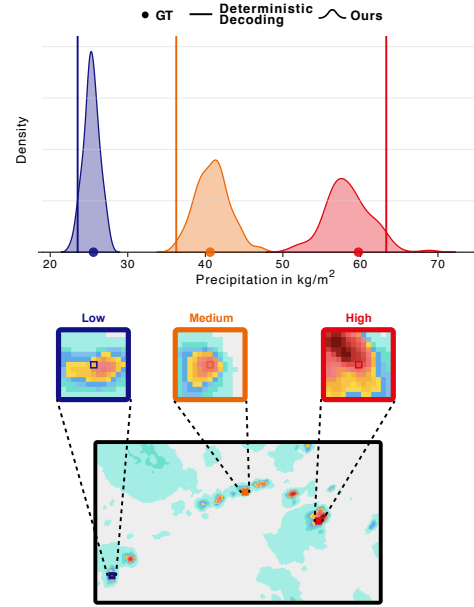


Figure 1. **Reconstruction ensemble distributions** from our generative compression stage for locations with medium (blue), heavy (orange), and extreme (red) precipitation. In light-rain regions, the ensemble shows low variance, while under intense and chaotic rainfall, the spread increases and reliably covers the ground-truth values (dots), whereas the deterministic CasCast decoder [40] (lines) cannot quantify uncertainty and fails to cover ground truth.

Uncertainty quantification is of particular importance in safety-critical settings where the range of plausible outcomes matters more than the most likely one. Early generative approaches use Generative Adversarial Networks (GANs) [41, 79, 107, 158]. However, GANs suffer from training instabilities and mode collapse [66], limiting coverage of rare but critical long-tail events. Hence, effective nowcasting requires *data-driven methods* that are *accurate*, *probabilistic*, *fast*, and *scalable*.

Diffusion and flow-based models [3, 4, 50, 78, 80, 110, 126, 127] overcome GAN instabilities and mode collapse, but iterative sampling in high-dimensional spaces is computationally expensive. Commonly, a two-stage setup is employed to reduce overhead. First, a compression stage ab-

stracts imperceptible details. Second, a generative model operates in the learned latent space. While effective for natural images and videos, the current *two-stage design is ill-posed for weather forecasting*. Compression is inherently lossy, and errors that are imperceptible in images may correspond to substantial shifts in predicted precipitation. Two-stage modeling thus undermines reliability in safety-critical settings. Moreover, training such autoencoders requires balancing regularization [65], perceptual [157], and adversarial losses [41, 110], where the adversarial components can reintroduce instability and degrade coverage of extreme events. Despite these drawbacks, recent nowcasting models [37, 40, 71] continue to rely on this architecture to manage the high dimensionality of weather data.

In this work, we introduce a novel and simple first stage design, tailored to weather nowcasting. Replacing the standard decoder with a rectified flow decoder ensures that predictions are sharp and realistic, without adversarial or perceptual losses. Therefore, the compression stage becomes (1) easy to train, (2) scalable, and (3) able to quantify uncertainty in the decoding process. To ensure a smooth and well-behaved latent space, we introduce a novel stochastic tanh regularization, which restricts latents to the range $[-1, 1]$. Unlike KL regularization [65], it requires no loss weighting or architectural changes [65, 110]. We further propose an asymmetric architecture for our first stage, tailored for forecasting. In line with recent image synthesis works [43, 161], we utilize transformers for the first-stage encoder and decoder, thereby avoiding the inefficient convolutional design [161]. For latent-space forecasting, we must avoid *information leakage from future to past* frames, making sequence-level encoders [75, 133, 142, 150, 159] unsuitable. At the same time, we require frame-wise encoding [37, 40, 74] to support incremental updates and robustness to frame drops. However, purely frame-wise designs introduce flickering and *temporal inconsistency* [149].

We therefore propose *FREUD*, a **FR**ameworkwise **E**ncoder and **U**nited **D**ecoder architecture. Each frame is encoded independently by a lightweight transformer, while a hierarchical rectified flow transformer [24, 84, 99] decodes them jointly. *FREUD* provides a fast, scalable first stage for latent-space generation and yields temporally consistent reconstructions without adversarial training or loss weighting.

Prior diffusion-based nowcasting models either use a *fixed conditioning window* [37, 40, 71], which is vulnerable to missing or corrupted frames [2, 25, 63], or generate future frames auto-regressively [62, 103], which accumulates errors over time. Robust nowcasting therefore requires flexible, adaptive conditioning.

We achieve this through masking-based diffusion forcing [16, 54]. This allows inference with any number of conditioning frames and maintains strong skill even with only two past frames. Recent methods cascade a determin-

istic forecast with a generative model [40, 98, 153], improving localization but yielding overconfident predictions. We condition solely on observed precipitation, achieving better calibration. Combining this insight with our novel *FREUD* compression stage and masking-based rectified flow training yields state-of-the-art precipitation nowcasting on the SEVIR benchmark [139]. Our compact model outperforms prior work in Continuous Ranked Probability Score (CRPS) and perceptual metrics, while maintaining competitive localization without biasing the generation. We formulate our contributions as follows:

- **A simple, scalable first stage tailored for weather nowcasting.** We introduce a rectified-flow encoder-decoder with novel stochastic tanh-regularization that achieves higher reconstruction quality without perceptual or adversarial losses, ensuring a smooth, bounded latent space.
- **Frame-wise encoder and united video decoder.** We propose an asymmetric design that encodes frames independently to prevent information leakage and support variable-length inputs, while jointly decoding all frames simultaneously for temporal consistency.
- **Decoding uncertainty quantification.** Our probabilistic decoder design enables multiple reconstructions from the same latent, providing natural estimates of decoding uncertainty, crucial for safety-critical applications.
- **Scalable and robust latent-space nowcasting.** We achieve state-of-the-art precipitation forecasting through masking-based rectified-flow training that handles variable-length conditioning and frame drops, while scaling with model size, ensemble count, and function evaluations to trade latency for accuracy.

2. Related Works

Precipitation Nowcasting Classical Numerical Weather Prediction (NWP) is computationally expensive, making short-term nowcasts difficult [20, 71, 107, 120, 121, 125]. Optical-flow extrapolation methods [22, 39, 114, 146, 147] are faster but cannot capture the formation of new weather patterns [58, 120]. These issues motivate deep-learning approaches, categorized as deterministic or probabilistic. Deterministic models learn spatio-temporal mappings from past to future precipitation [1, 35, 36, 42, 120, 144]. However, they often yield blurry forecasts due to regression losses and also lack uncertainty quantification [37, 71, 90, 107]. Probabilistic approaches use GANs [79, 107, 158] or diffusion models (DMs) [37, 40, 71, 77, 90, 98] to generate weather predictions, producing sharp samples and estimating uncertainty via Monte-Carlo (MC) sampling. Mode collapse and training instabilities limit GANs [66], making diffusion models the state of the art [37, 40, 71, 153]. Many methods operate in the latent space of a compression autoencoder [37, 40, 71], but ignore compression uncertainty [77]. Moreover, deterministic conditioning [40, 97,

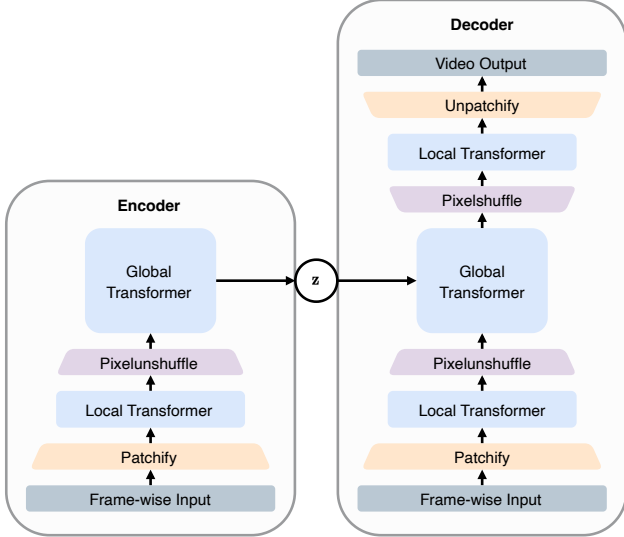


Figure 2. **FREUD architecture.** *Left:* Frame-wise encoder. *Right:* Generative decoder conditioned on encoder latents z .

[153], often biases the generation [98]. We address these issues with a first stage that quantifies compression uncertainty and enables purely data-driven nowcasting. Further discussion of related works is provided in the Appendix.

Uncertainty Estimation in ML differentiates uncertainty from underdeterminedness of the problem (aleatoric uncertainty) or underspecification of the model (epistemic uncertainty) [57]. Aleatoric uncertainty is important in weather nowcasting due to non-linearities in the atmospheric system [53, 71, 90, 118]. Traditionally, Bayesian Neural Networks [85, 86], MC Dropout [34, 129], and model ensembling [67] are used to estimate uncertainty but are either impractical for large generative models or degrade performance [137]. DMs allow zero-shot aleatoric uncertainty quantification [14, 122] by sampling multiple times given the same conditioning. The variance of this ensemble serves as an estimate of aleatoric uncertainty [14, 37, 71, 90].

Diffusion Autoencoders (DiffAEs) replace the deterministic decoder with a generative model conditioned on encoder outputs [101]. Previous work uses discretized [8, 9, 117, 155] as well as continuous [11, 21, 56, 160] latent encodings to enable downstream generation in the latent space [9, 11, 21, 56, 117, 160]. Compared to standard VAEs, DiffAEs yield better detail reconstruction for images and more stable training [21, 160]. Earlier video generation methods use frame-wise compression [6, 12, 38, 46, 83, 123, 143], causing temporal inconsistencies [149, 159], or 3D encoder-decoder models [75, 133, 135, 142, 154], with limited capacity [159]. Concurrent DiffAE-based video compressors [150, 159] achieve superior reconstructions over VAE baselines with few sampling steps and strong generative downstream performance. We improve upon these

approaches by using a hierarchical Transformer-based architecture, unlocking scalable performance, and introducing a novel regularization. Moreover, our design better suits forecasting by avoiding perceptual losses, encoding frames independently, and assessing reconstruction uncertainty.

3. Method

In the following, we consider sequences of precipitation maps $\mathbf{x}^t \in \mathbb{R}^{C \times H \times W}$, where C , H , and W denote channels, height, and width, respectively. The superscript t indexes time frames, and the subscript i denotes diffusion steps \mathbf{x}_i . Given the L^{in} previous precipitation maps, the task is to predict the next L^{out} frames. As we cannot model the chaotic nature of precipitation deterministically, we sample from the conditional distribution $p(\mathbf{x}^{\text{out}}|\mathbf{c})$ of possible future precipitation using a generative model. We follow previous work and cast the precipitation nowcasting problem as a probabilistic spatio-temporal prediction task [35, 37, 153]. Hence, future frames \mathbf{x}^{out} are sequences of L^{out} precipitation maps while the conditioning \mathbf{c} are L^{in} previous frames.

3.1. Preliminary

Rectified Flow Generative models that transform noise into data have recently gained significant attention, particularly diffusion- [50, 110, 126, 127] and flow-based models [3, 4, 19, 27, 78, 80]. *Rectified Flows* (RF) [32, 80] or *Stochastic Interpolants* [3, 4, 84] generalize these frameworks by mapping samples $\mathbf{x}_0 \sim p_0$ from a simple prior (typically $\mathcal{N}(0, \mathbf{I})$) to data samples $\mathbf{x}_1 \sim p_1$ through the continuous interpolation $\mathbf{x}_i = \alpha_i \mathbf{x}_1 + \sigma_i \mathbf{x}_0$, where α_i increases and σ_i decreases over time, controlling the transition from noise to data. The velocity field is defined as

$$\mathbf{v}(\mathbf{x}_i, i) = \frac{d\mathbf{x}_i}{di} = \dot{\alpha}_i \mathbf{x}_1 + \dot{\sigma}_i \mathbf{x}_0 \quad (1)$$

where $\dot{\alpha}_i$ and $\dot{\sigma}_i$ are time derivatives of α_i and σ_i . This induces a probability flow ODE whose marginal distribution at time i equals $p_i(\mathbf{x})$. Following prior work [32, 78, 84], we adopt the linear interpolant $\alpha_i = i$, $\sigma_i = 1 - i$. A neural network $\mathbf{v}_\theta(\mathbf{x}_i, i)$ with parameters θ is trained to predict the velocity field by minimizing

$$\mathcal{L}_\mathbf{v}(\theta) = \int \mathbb{E}[\|\mathbf{v}_\theta(\mathbf{x}_i, i) - (\dot{\alpha}_i \mathbf{x}_1 + \dot{\sigma}_i \mathbf{x}_0)\|^2] di. \quad (2)$$

After training, samples from the prior are transported to the data distribution by numerically integrating the ODE with $\mathbf{v}_\theta(\mathbf{x}_i, i)$ using standard solvers, e.g., Euler integration.

Uncertainty Quantification Following Chan et al. [14], we consider the atmosphere to be a dynamic system $\mathbf{x}^{\text{out}} = \mathcal{F}(\mathbf{c}) + \eta$ with deterministic dynamics $\mathcal{F}(\mathbf{c})$ and irreducible or unmodeled noise η . Even if we can perfectly capture the deterministic dynamics of the system $\mathcal{F}(\mathbf{c})$, there remains

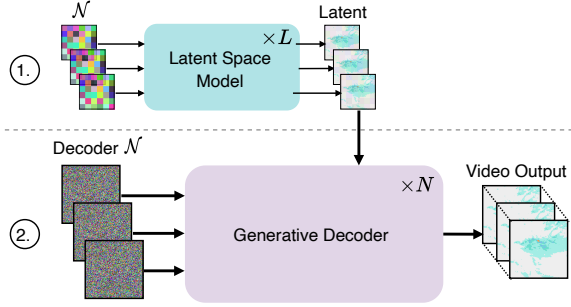


Figure 3. **Inference pipeline.** We first generate weather forecasts in the latent space of our FREUD encoder and then decode the predictions with our generative FREUD decoder.

an error because of the stochastic component. Therefore, if we can draw Monte-Carlo samples $\mathbf{x}_e^{\text{out}}$ from the distribution, the sample variance

$$\text{Var}(\bar{\mathbf{x}}^{\text{out}}), \quad \bar{\mathbf{x}}^{\text{out}} = [\mathbf{x}_e^{\text{out}}]_{e=0}^N, \quad \mathbf{x}_i^{\text{out}} \sim p(\mathbf{x}^{\text{out}}|\mathbf{c}) = \mathcal{F}(\mathbf{c}) + \eta \quad (3)$$

where the subscript \cdot_e indexes independently sampled ensemble members, will converge to the irreducible aleatoric uncertainty $\text{Var}(\eta)$ for $N \rightarrow \infty$ [14]. As we can approximate $p(\mathbf{x}^{\text{out}}|\mathbf{c})$ using a generative model, we can estimate the uncertainty by computing N probabilistic predictions and calculating the ensemble variance [14, 71, 90, 118].

3.2. FREUD

Diffusion- and flow-based generative methods iteratively sample in data space, which is particularly costly for high-resolution weather data. Therefore, following prior work on image and video synthesis, we perform generative modeling in a compressed latent space, which substantially reduces computational complexity [40, 71, 110, 110, 135].

For operational weather nowcasting, a first-stage encoder–decoder should fulfill several key properties. First, **training should be simple and stable**, avoiding adversarial or perceptual objectives. Second, the model must offer **efficient compression** of high-dimensional radar. Third, its latent space should be **smooth and well-structured**, amenable to generative modeling. Fourth, the model should enable **uncertainty estimation** in the decoding process, an essential property for safety-critical applications. Fifth, **frame-wise encoding** is desirable to ensure robustness to sensor faults or dropped frames, common in radar networks. Finally, outputs must be **temporally coherent**, since flickering reconstructions across frames would lead to inconsistencies in subsequent forecasts. They motivate our design of the FREUD framework, which features an architecture that provides efficient compression, robustness to sensor faults, and temporally coherent reconstructions.

Architecture Fig. 2 shows our FREUD architecture. To ensure efficiency, we follow recent works [43, 161] and use a fully transformer-based encoder-decoder design.

Encoder. The encoder is implemented as a lightweight transformer that operates frame-wise, allowing each frame to be processed independently. This makes the model robust to missing or corrupted radar frames, which are common in operational weather sensing, and enables online updates as new frames become available without requiring re-encoding of the entire sequence. The frame-wise design further prevents information leakage from future to past frames, which sequence-level encoders would suffer from, thereby preserving the causal structure essential for forecasting.

Decoder. For decoding, we use a transformer-based video decoder that jointly reconstructs all frames to ensure temporal consistency. To cope with the high computational cost of attention in large video tensors, we follow *Hourglass diffusion transformers* [24], and adopt a hierarchical transformer architecture. Here, the spatial resolution is progressively reduced and later restored through pixel-unshuffle and pixel-shuffle operations, which rearrange spatial dimensions into channel dimensions (and vice versa) [119]. We condition the decoder on the encoder latents by concatenating them channel-wise in the bottleneck, guiding the video reconstruction process through the encoded spatial representations. We further improve efficiency through space-time factorized attention [44]. Each block alternates between spatial and temporal attention, followed by a feed-forward network. Spatial attention attends to all tokens within each frame, and temporal attention attends to all tokens in the same spatial positions across all frames.

Finally, we further reduce complexity in high-resolution stages by integrating neighborhood attention [45], which restricts self-attention to local spatial neighborhoods rather than full global context.

Training Paradigm Previous works train autoencoders with a small KL regularization to encourage a smooth latent space, and additional perceptual and adversarial losses to boost sharpness [40, 71, 110]. However, these objectives require careful loss balancing [21, 150, 159, 160], and adversarial training often leads to training instability and mode collapse, while both perceptual and adversarial losses can suppress subtle yet safety-critical details [66, 77]. Moreover, their decoders are deterministic at inference, providing no estimate of decoding uncertainty. We address these limitations by training our first stage with the rectified flow (RF) loss from Eq. (2). Optimization with this loss is stable and makes perceptual and adversarial objectives obsolete, greatly simplifying training. It further allows us to sample from our decoder during inference, which naturally provides an empirical way to quantify decoding uncertainty through multiple reconstructions. We condition the decoder on the frame-wise latents and train both the encoder and

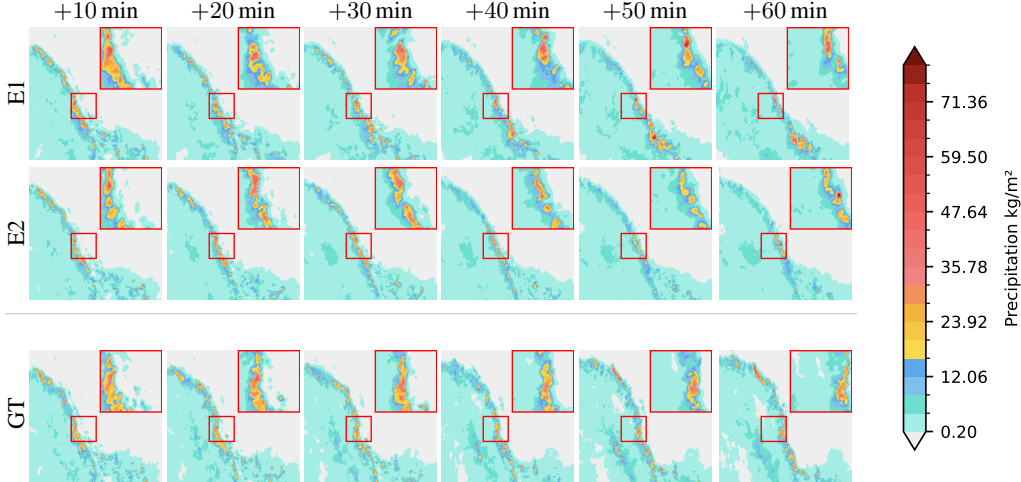


Figure 4. **Forecast ensemble** from our L model. Red rectangles show zoom-ins to highlight differences. Best viewed zoomed in.

decoder jointly with the RF loss from Eq. (2).

Latent Space Regularization A well-structured latent space is essential for latent space generative modeling [43, 152, 161]. Current autoencoders typically include a small KL regularization term to encourage a smooth latent space [110]. In contrast, our framework does not inherently constrain the latent space, leading to high variance and low density. Thus, in addition to the *unregularized (unreg.)* case, we introduce and ablate two additional regularization schemes to ensure robust latent representations.

KL-regularization (KL-reg.), as used in latent diffusion autoencoders [110], penalizes the divergence between the latent distribution and a standard normal. This encourages smoother and more robust latent representations but introduces a trade-off: stronger KL weights improve regularization at the cost of reconstruction fidelity, requiring loss balancing. Moreover, it requires architectural modifications, as the encoder must predict both the mean and the standard deviation per latent dimension.

Stochastic tanh regularization (T-reg.). We propose *T-reg.* as a simple yet effective alternative to KL-based regularization that achieves all desired properties of a well-behaved latent space: bounded, smooth, and amenable to generation. We constrain the latent values to $[-1, 1]$ via a tanh activation and add a small Gaussian perturbation $\epsilon \sim \mathcal{N}(0, \sigma^2 \mathbf{I})$ with variance σ^2 to the latent representation, so that

$$\tilde{\mathbf{z}}^t = \tanh(\text{Enc}_\theta(\mathbf{x}^t)) + \sigma\epsilon \quad (4)$$

where Enc_θ denotes the frame-wise FREUD encoder and \mathbf{x}^t the input frame. This stochastic perturbation makes nearby latents decode into similar pixel-space videos, encouraging smoothness and robustness to small changes in the latent space. Unlike KL regularization, *T-reg.* acts purely as an architectural constraint rather than an additional loss, eliminating the need for loss balancing. The final loss for training

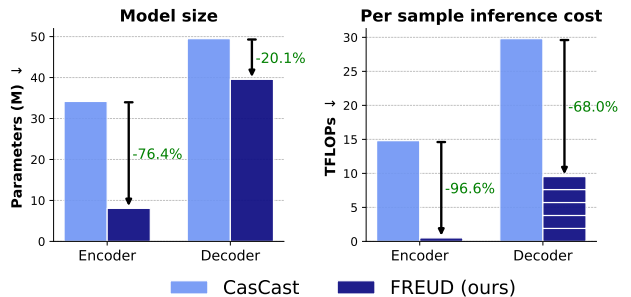


Figure 5. **FREUD efficiency.** Our transformer-based autoencoder has fewer parameters and uses fewer FLOPs for encoding and decoding (5 NFE). This allows for faster training and inference.

the FREUD first stage with *T-reg.* is thus just the flow loss from Eq. (2), simplified with the linear schedule to

$$\mathcal{L} = \|\mathbf{v}_\theta(\mathbf{x}_i, i) - (\mathbf{x}_1 - \mathbf{x}_0)\|^2 \quad (5)$$

where \mathbf{x}_1 is a data sample and $\mathbf{x}_0 \sim \mathcal{N}(0, \mathbf{I})$. Similar to [135], we find that a simple outlier punishment is helpful in early training (for details see Appendix).

3.3. Latent Space Nowcasting

With FREUD as our first stage, we perform nowcasting directly in its latent space. Its frame-wise encoder tolerates missing frames, so our latent model must likewise support variable-length conditioning and remain robust under limited past observations. For this we adopt a masking-based training strategy, which teaches the model to infer future dynamics from arbitrary subsets of past frames and allows flexible conditioning lengths during inference, ensuring resilience to missing or corrupted frames.

Training We follow the simple training paradigm of RaMViD [54], where we randomly mask part of each

clip and learn to denoise the remaining part. More formally, we split a video of length $T = L^{\text{in}} + L^{\text{out}}$ into conditioning frames $\mathbf{x}_1^{\mathcal{C}}$ and generation frames $\mathbf{x}_1^{\mathcal{G}}$ where $\mathcal{C} \cup \mathcal{G} = \{0, \dots, T-1\}$ and $\mathcal{C} \cap \mathcal{G} = \emptyset$. The final video is given by $\mathbf{x}_1 = \mathbf{x}_1^{\mathcal{C}} \oplus \mathbf{x}_1^{\mathcal{G}}$ where \oplus is a frame selection operation. For every sample we draw k conditioning indices uniformly from $\{1, \dots, K\}$, where the hyperparameter $K < T$ defines the maximum number of conditioning frames. Only the remaining frames with indices in $\mathcal{G} = \{0, \dots, T-1\} \setminus \mathcal{C}$, are noised, so the model input is $\mathbf{x}_i = \mathbf{x}_1^{\mathcal{C}} \oplus \mathbf{x}_i^{\mathcal{G}}$. Randomising the amount of conditioning $|\mathcal{C}| = k$ during training teaches the model to leverage any variable subsets of information to make its predictions. We compute the loss from Eq. (2) only on noisy frames $\mathbf{x}_i^{\mathcal{G}}$. Similar to [54] we define probability p_U with which we train fully unconditional, i.e., set $\mathcal{C} = \emptyset$. This enables classifier-free guidance [48].

Inference At inference we encode the latest L^{in} available observations with the frame-wise encoder and append L^{out} Gaussian latent frames $\mathbf{x}_0^t \in \mathbb{R}^{C_i \times H_i \times W_i}$. This yields a sequence of $T = L^{\text{in}} + L^{\text{out}}$ latent frames, consisting of conditioning latents and noisy targets. The latent rectified flow model then denoises this sequence, and the FREUD decoder maps the denoised latents back to pixel space, producing a forecast for the L^{out} future frames. See Fig. 3 for an overview of the full pipeline. To estimate predictive uncertainty, we form latent-space ensembles by resampling the L^{out} with fixed conditioning. Additionally, we can generate decoder ensembles by rerunning the decoding process with different noise initializations for the same latent sequence.

4. Experiments

Following prior work [35, 40], we evaluate our method on the SEVIR benchmark [139], which consists of 20,393 (extreme) weather events, collected from 2017 to 2019. Each event covers a 384×384 km region for a 4 h timespan. Vertically Integrated Liquid (VIL) from the NEXRAD radar mosaic indicates precipitation and is recorded with 1 km spatial and 5 min temporal resolution. We provide more details on the SEVIR dataset, the computational resources used for experiments, as well as additional experiments on the MeteoNet benchmark [70] in the Appendix.

4.1. FREUD First Stage

First, we evaluate our frame-wise encoder and joint decoder architecture. We follow prior work [21, 150, 159, 160] and report RMSE, MAE, SSIM, and PSNR. We capture temporal smoothness with the MAE of discrete time derivatives (dMAE), and overall predictive uncertainty by the variance (Var) over ensemble members, as defined in Sec. 3.1.

Reconstruction Performance We report reconstruction metrics for FREUD and the prior state-of-the-art frame-wise autoencoder CasCast [40] in Tab. 1. Our T -

Table 1. **Reconstruction performance** of the framewise CasCast autoencoder, a framewise Diffusion Autoencoder, and FREUD variants with different regularization.

| Model | Ens. | RMSE ↓ | MAE ↓ | SSIM ↑ | PSNR ↑ | dMAE ↓ |
|--------------|------|--------------|--------------|--------------|---------------|--------------|
| CasCast [40] | – | 0.022 | 0.008 | 0.976 | 39.153 | 0.012 |
| T-reg. | 1 | 0.027 | 0.011 | 0.970 | 37.415 | 0.015 |
| DiffAE | 10 | 0.025 | 0.010 | 0.974 | 38.13 | 0.012 |
| unreg. | 1 | 0.027 | 0.009 | 0.989 | 37.550 | 0.013 |
| FREUD | 10 | 0.023 | 0.008 | 0.987 | 38.915 | 0.012 |
| KL-reg. | 1 | 0.025 | 0.009 | 0.992 | 37.927 | 0.013 |
| FREUD | 10 | 0.022 | 0.008 | 0.987 | 39.029 | 0.011 |
| T-reg. | 1 | 0.019 | 0.008 | 0.998 | 40.224 | 0.011 |
| FREUD | 10 | 0.018 | 0.007 | 0.999 | 41.085 | 0.010 |

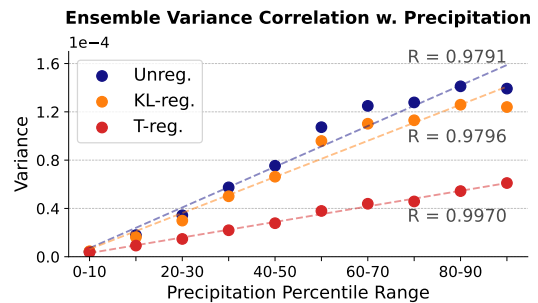


Figure 6. **Correlation between precipitation intensity and decoding variance.** All FREUD variants show a strong linear relationship, with T -reg. achieving the highest correlation.

reg. FREUD achieves superior results across all metrics, with a significant gain in SSIM, indicating perceptually accurate reconstructions without adversarial or perceptual losses. It further needs fewer parameters and fewer Floating Point Operations (FLOPs) than the CasCast autoencoder, as shown in Fig. 5. Encoding is 96%, while decoding is 68% faster with five NFE. This efficiency pays off twice: fast encoding accelerates latent-space model training, while efficient encoding and decoding enable rapid forecast updates during inference, which is crucial for operational nowcasting. In summary, FREUD is not only easier to train, but also more compute-efficient, and delivers higher-fidelity reconstructions, even with only one ensemble member.

Decoding Uncertainty Through the generative decoder, FREUD can sample multiple realizations given the same conditioning. As described in Sec. 3.1, we estimate decoding uncertainty from the variance across reconstructions. Fig. 7 shows a five-member ensemble of FREUD for both normal and extreme weather events along with corresponding ensemble variance maps. While reconstructions are highly similar overall, they differ in small-scale structures, particularly in regions of intense precipitation. Unlike natural image synthesis, where such variations are imperceptible, in weather forecasting they reflect genuine differences

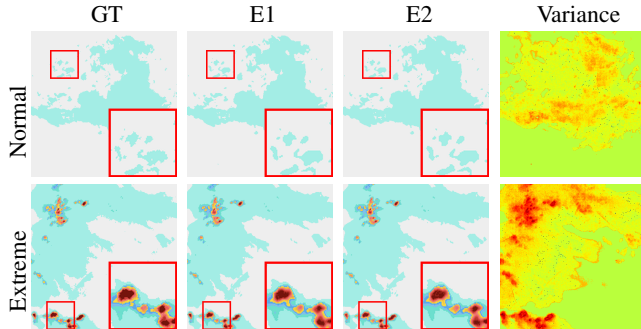


Figure 7. **Qualitative reconstructions** of a normal and an extreme weather event, with corresponding ensemble members and ensemble variance. The red rectangle highlights a zoomed-in area for visualizing differences in details. Best viewed zoomed in.

in high-impact regions. The variance maps reveal a clear correlation between precipitation intensity and reconstruction variance, consistent with the non-linearity and chaotic dynamics of severe weather. This shows that ensemble-based reconstructions capture meaningful variability precisely in regions of heightened uncertainty, providing valuable insight for safety-critical extreme events. Fig. 6 further confirms a strong linear relationship between precipitation percentile and intra-ensemble variance across all FREUD variants, with the *T-reg.* model showing the highest correlation ($r = 0.997$). In summary, these findings confirm that first-stage ensembling effectively identifies dynamically complex weather, providing meaningful and spatially localized uncertainty estimates. Additional experiments inserting abnormal patterns, similar to [14], and more qualitative results are presented in the Appendix.

4.2. Forecasting performance

Given the FREUD first stage, we train a latent space model for forecasting. We follow prior works [35, 40] and use $L^{\text{in}} = 13$ frames (65 min) of previous precipitation to predict the next $L^{\text{out}} = 12$ frames (60 min). Unless specified otherwise, we use ten forecasting ensemble members similar to prior work [37, 40, 71, 153]. We use the evaluation pipeline provided by Gong et al. [40] and evaluate probabilistic nowcasting performance with the Continuous Ranked Probability Score (CRPS), perceptual realism with the Structural Similarity Index Measure (SSIM), and report Heidke Skill Score (HSS) and Critical Success Index (CSI). HSS expresses improvement over random chance, with 1 indicating a perfect forecast and 0 indicating no improvement over guessing. CSI quantifies the hit rate while ignoring true negatives, making it robust when no events dominate. Both scores are averaged across six precipitation/no precipitation thresholds. We provide more details in the Appendix.

State-of-the-Art Comparison Tab. 2 quantitatively compares our method to current state-of-the-art weather now-

Table 2. **SEVIR benchmark** comparison of our method with various deterministic and probabilistic models. Baselines are sourced from CasCast [40]. For † the model is trained on a downsampled dataset with a size of 128 since they found that training on the original dataset does not yield high-quality predictions.

| Method | CRPS↓ | SSIM↑ | HSS↑ | CSI↑ |
|--------------------------------|---------------|---------------|---------------|---------------|
| ConvLSTM [120] (NeurIPS '15) | 0.0264 | 0.7749 | 0.5232 | 0.4102 |
| PredRNN [144] (TPAMI '22) | 0.0271 | 0.7497 | 0.5192 | 0.4045 |
| PhyDNet [42] (CVPR '20) | 0.0253 | 0.7649 | 0.5311 | 0.4198 |
| SimVP [36] (CVPR '22) | 0.0259 | 0.7772 | 0.5280 | 0.4153 |
| EarthFormer [35] (NeurIPS '22) | 0.0251 | 0.7756 | 0.5411 | 0.4310 |
| NowcastNet [158] (Nature '23) | 0.0283 | 0.5696 | 0.5365 | 0.4152 |
| PreDiff† [37] (NeurIPS '23) | 0.0202 | 0.7648 | 0.4914 | 0.3875 |
| CasCast [40] (ICML '24) | 0.0202 | 0.7797 | 0.5602 | 0.4401 |
| FREUD + LSM-L (ours) | 0.0190 | 0.7841 | 0.5011 | 0.3864 |
| ↳ with cfg | 0.0192 | 0.7937 | 0.5537 | 0.4277 |

casting methods on the SEVIR benchmark. Our Large Latent Space Model (LSM-L) combined with the *T-reg.* FREUD first stage achieves state-of-the-art CRPS and SSIM, outperforming all existing methods in both distribution coverage and perceptual quality. Our method provides significant gains, given that improvements on SEVIR are typically small. For instance, CasCast [40] improves over PreDiff [37] by 0% CRPS and +1.95% SSIM, whereas our method improves over CasCast by +5.94% CRPS and +1.80% SSIM. CasCast reports its state-of-the-art results using Classifier-Free Guidance (CFG) [48], which also improves localization metrics in our model. With CFG, our method becomes competitive on HSS and CSI, being only outperformed by CasCast on HSS. However, we observe that CFG systematically increases predicted precipitation for both CasCast and our method, suggesting that CFG-based improvements in localization may stem from this simple shift rather than better modeling. We therefore consider CFG to be flawed for nowcasting and further ablate its effects in the Appendix. Qualitative results in Fig. 4 show that our predictions are visually consistent with the ground truth and capture realistic variations in localized precipitation patterns. We provide more samples in the Appendix.

Calibration Similar to previous work [13, 71, 73], we use ensemble rank histograms to assess calibration: a uniform shape indicates well-calibrated uncertainty, whereas a U-shape reflects overconfidence. As shown in Fig. 8, our ensemble is substantially closer to uniform, indicating better calibration. In contrast, CasCasts rank histogram indicates strong overconfidence. Quantitative assessment via the reliability index (RI) [26, 145], with 1,000 bootstrap resamples to compute a 95% confidence interval, confirms our approach achieves a significantly better reliability error ($RI = 0.135 \pm 0.001$) than CasCast ($RI = 0.312 \pm 0.001$).

Scalability We show the scalability of our approach by training models of different sizes, with quantitative results

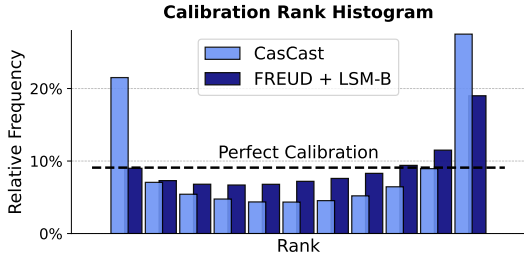


Figure 8. **Calibration Rank Histogram** for our pipeline. Our rank histogram is flatter, indicating improved calibration compared to CasCast [40].

Table 3. **Scaling Analysis** of the forecasting latent space flow model. Localization metrics and CRPS consistently improve with larger model sizes. All models outperform CasCast for CRPS.

| Model | Num. Params | CRPS ↓ | SSIM ↑ | HSS ↑ | CSI ↑ |
|--------------|-------------|---------------|---------------|---------------|---------------|
| CasCast [40] | 309M | 0.0202 | 0.7797 | 0.5602 | 0.4401 |
| Ours LSM-S | 44M | 0.0200 | 0.7742 | 0.4514 | 0.3485 |
| ↳ with cfg | | 0.0201 | 0.7887 | 0.5155 | 0.3962 |
| Ours LSM-B | 141M | 0.0196 | 0.7828 | 0.4923 | 0.3805 |
| ↳ with cfg | | 0.0204 | 0.7987 | 0.5256 | 0.4041 |
| Ours LSM-L | 473M | 0.0190 | 0.7841 | 0.5011 | 0.3864 |
| ↳ with cfg | | 0.0192 | 0.7937 | 0.5537 | 0.4277 |

Table 4. **Training-free deterministic conditioning.** Localization performance on SEVIR improves when introducing deterministic priors while distribution coverage deteriorates. $i = 1$ corresponds to a fully deterministic and $i = 0$ to a fully generative prediction.

| Model | det. prior | i | CRPS ↓ | HSS ↑ | CSI-M ↑ |
|-------------|------------|------|---------------|---------------|---------------|
| Earthformer | na | na | 0.0251 | 0.5411 | 0.4310 |
| CasCast | ✓ | na | 0.0202 | 0.5602 | 0.4401 |
| | ✗ | 0 | 0.0190 | 0.5011 | 0.3864 |
| | ✓ | 0.2 | 0.0198 | 0.5714 | 0.4444 |
| Ours | ✓ | 0.5 | 0.0219 | 0.5735 | 0.4455 |
| | ✓ | 0.75 | 0.0233 | 0.5598 | 0.4338 |

reported in Tab. 3. Similar to trends observed in image synthesis, we find that larger latent-space models consistently improve performance across all metrics. Notably, even our smallest model (LSM-S) achieves competitive performance despite using only a fraction of the parameters of prior work. Our largest model (LSM-L) achieves the best overall results, confirming that our approach scales favorably with model capacity.

Deterministic Prior We achieve top-3 CSI and 2nd-best HSS without deterministic priors. However, our training paradigm allows zero-shot deterministic conditioning by initializing future frames with noisy Earthformer [35] predictions, where the noise level allows to express confidence in the deterministic prediction. Conditioning on these reduces diversity by lowering conditional variance, which improves localization of mean predictions if correct but col-

Table 5. **Comparison of B-LSMs** in our regularized latent spaces. T -reg. outperforms $unreg.$ and KL -reg. in terms of CRPS and SSIM but performs worse for localization metrics.

| Regularization | CRPS ↓ | SSIM ↑ | HSS ↑ | CSI ↑ |
|----------------|---------------|---------------|---------------|---------------|
| Unreg. | 0.0222 | 0.7630 | 0.5139 | 0.3956 |
| KL-reg. | 0.0201 | 0.7790 | 0.4993 | 0.3892 |
| T -reg. | 0.0196 | 0.7828 | 0.4923 | 0.3805 |

lapses the distribution to incorrect modes otherwise. Tab. 4 confirms this trade-off: relying on deterministic predictions allows better localization but worse coverage.

4.3. Ablations

Regularization As shown in Tab. 1, T -reg. FREUD delivers the best reconstruction quality and the most meaningful uncertainty estimates (Fig. 6). T -reg. also produces a more compact and structured latent space (see Appendix), whereas other variants exhibit higher variance and lower density. Tab. 5 shows that this improved structure translates into better downstream performance: B-LSMs trained on T -reg. latents achieve superior CRPS and SSIM compared to those trained on other latent spaces.

Joint Video Decoding We ablate the effect of united (joint) decoding in Tab. 1. While a frame-wise DiffAE is competitive with the frame-wise CasCast autoencoder [40], it performs noticeably worse than FREUD. Using the same regularization settings, FREUD reduces dMAE by 33%, indicating improved temporal consistency. Qualitative video samples in the supplementary material further confirm this effect: frame-wise decoding exhibits small fluctuations and flickering artifacts, whereas united decoding produces smoother and more temporally stable reconstructions.

5. Conclusion

We introduce FREUD, a simple and scalable first-stage compression framework. FREUD is built on a frame-wise transformer encoder and a probabilistic rectified-flow video decoder. This design eliminates the need for perceptual or adversarial losses, produces sharper and more stable reconstructions, and, most importantly, allows for direct uncertainty estimation at the decoding stage. When combined with a latent-space rectified-flow transformer, our pipeline achieves state-of-the-art precipitation nowcasting on SEVIR. It offers strong calibration, flexible conditioning, and favorable scaling with model size, ensemble size, and test-time computation. By capturing first- and second-stage uncertainties while remaining purely data-driven, our approach paves the way for reliable short-term precipitation forecasting, without relying on deterministic physics-based predictors. We discuss remaining limitations and potential societal impacts in the Appendix.

Acknowledgments

We would like to thank Carla Sagebiel for proposing the framework name, Dominik Lorenz for initiating the project, Owen Vincent for the technical support, and Marius Jacobs & Nadja Sauter for their preliminary experiments. This project has been supported by the bidt project KLIMA-MEMES, the Horizon Europe project ELIOT (GA No. 101214398), the project “GeniusRobot” (01IS24083) funded by the Federal Ministry of Research, Technology and Space (BMFTR), the BMW ZIM-project (No. KK5785001LO4) “conIDditional LoRA”, and the German Federal Ministry for Economic Affairs and Energy within the project “NXT GEN AI METHODS - Generative Methoden für Perzeption, Prädiktion und Planung”. The authors gratefully acknowledge the Gauss Center for Supercomputing for providing compute through the NIC on JUWELS/JUPITER at JSC and the HPC resources supplied by the NHR@FAU Erlangen.

Author Contributions

JS and JW jointly lead the project, conceptualized the core methodology, and preprocessed the data. JS conceived the initial idea and devised initial prototypes. JW developed, optimized, and evaluated the final models. NS provided an initial implementation of Diffusion Autoencoders and contributed to figure design. TP conceptualized the stochastic tanh regularization method and conducted initial comparisons of regularization. All authors contributed to writing. BO supervised the project and reviewed the manuscript.

References

- [1] Shreya Agrawal, Luke Barrington, Carla Bromberg, John Burge, Cenk Gazen, and Jason Hickey. Machine learning for precipitation nowcasting from radar images. *arXiv preprint arXiv:1912.12132*, 2019. 1, 2, 10, 11
- [2] Ali M. Al-Saegh, Taha A. Elwi, Osama A. Abdullah, Aduwati Sali, and Abdulmajeed H. J. Aljumaily. Rainfall Effect on Satellite Communications in Mosul at Frequencies above 10 GHz. In *2021 7th International Conference on Space Science and Communication (IconSpace)*, pages 318–322, 2021. 2
- [3] Michael Samuel Albergo and Eric Vanden-Eijnden. Building normalizing flows with stochastic interpolants. In *ICLR*, 2023. 1, 3
- [4] Michael S Albergo, Nicholas M Boffi, and Eric Vanden-Eijnden. Stochastic interpolants: A unifying framework for flows and diffusions. *arXiv preprint arXiv:2303.08797*, 2023. 1, 3
- [5] Ferran Alet, Ilan Price, Andrew El-Kadi, Dominic Masters, Stratis Markou, Tom R. Andersson, Jacklynn Stott, Remi Lam, Matthew Willson, Alvaro Sanchez-Gonzalez, and Peter Battaglia. Skillful joint probabilistic weather forecasting from marginals, 2025. 11
- [6] Jie An, Songyang Zhang, Harry Yang, Sonal Gupta, Jiabin Huang, Jiebo Luo, and Xi Yin. Latent-Shift: Latent Diffusion with Temporal Shift for Efficient Text-to-Video Generation, 2023. 3
- [7] Andrea Asperti, Fabio Merizzi, Alberto Paparella, Giorgio Pedrazzi, Matteo Angelinelli, and Stefano Colamonaco. Precipitation nowcasting with generative diffusion models, 2023. 11
- [8] Roman Bachmann, Oğuzhan Fatih Kar, David Mizrahi, Ali Garjani, Mingfei Gao, David Griffiths, Jiaming Hu, Afshin Dehghan, and Amir Zamir. 4M-21: An Any-to-Any Vision Model for Tens of Tasks and Modalities. In *The Thirty-eighth Annual Conference on Neural Information Processing Systems*, 2024. 3
- [9] Roman Bachmann, Jesse Allardice, David Mizrahi, Enrico Fini, Oğuzhan Fatih Kar, Elmira Amirloo, Alaaeldin El-Nouby, Amir Zamir, and Afshin Dehghan. FlexTok: Resampling Images into 1D Token Sequences of Flexible Length, 2025. 3
- [10] Gedas Bertasius, Heng Wang, and Lorenzo Torresani. Is Space-Time Attention All You Need for Video Understanding?, 2021. 7
- [11] James Betker, Gabriel Goh, Li Jing, † TimBrooks, Jianfeng Wang, Linjie Li, † LongOuyang, † JuntangZhuang, † JoyceLee, † YufeiGuo, † WesamManassra, † PrafullaDhariwal, † CaseyChu, † YunxinJiao, and Aditya Ramesh. Improving Image Generation with Better Captions. In *Computer Science*, 2023. 3
- [12] Andreas Blattmann, Robin Rombach, Huan Ling, Tim Dockhorn, Seung Wook Kim, Sanja Fidler, and Karsten Kreis. Align Your Latents: High-Resolution Video Synthesis with Latent Diffusion Models. In *2023 IEEE/CVF Conference on Computer Vision and Pattern Recognition (CVPR)*, pages 22563–22575, Vancouver, BC, Canada, 2023. IEEE. 3
- [13] Rüdiger Brecht and Alex Bihlo. Towards replacing precipitation ensemble predictions systems using machine learning. *Atmospheric Science Letters*, n/a(n/a):e1262, 2024. 7
- [14] Matthew A. Chan, Maria J. Molina, and Christopher A. Metzler. Hyper-Diffusion: Estimating Epistemic and Aleatoric Uncertainty with a Single Model, 2024. 1, 3, 4, 7
- [15] Boyuan Chen, Diego Marti Monso, Yilun Du, Max Simchowitz, Russ Tedrake, and Vincent Sitzmann. Diffusion forcing: Next-token prediction meets full-sequence diffusion, 2024. 6
- [16] Boyuan Chen, Diego Marti Monso, Yilun Du, Max Simchowitz, Russ Tedrake, and Vincent Sitzmann. Diffusion Forcing: Next-token prediction meets full-sequence diffusion, 2024. 2
- [17] Jieneng Chen, Jieru Mei, Xianhang Li, Yongyi Lu, Qihang Yu, Qingyue Wei, Xiangde Luo, Yutong Xie, Ehsan Adeli, Yan Wang, Matthew P. Lungren, Shaoting Zhang, Lei Xing, Le Lu, Alan Yuille, and Yuyin Zhou. TransUNet: Rethinking the U-Net architecture design for medical image segmentation through the lens of transformers. *Medical Image Analysis*, 97:103280, 2024. 10
- [18] Lei Chen, Fei Du, Yuan Hu, Zhibin Wang, and Fan Wang. SwinRDM: Integrate SwinRNN with Diffusion Model to-

- wards High-Resolution and High-Quality Weather Forecasting. *Proceedings of the AAAI Conference on Artificial Intelligence*, 37(1):322–330, 2023. 12
- [19] Ricky TQ Chen, Yulia Rubanova, Jesse Bettencourt, and David K Duvenaud. Neural ordinary differential equations. *Advances in neural information processing systems*, 31, 2018. 3, 11
- [20] Shengchao Chen, Guodong Long, Jing Jiang, Dikai Liu, and Chengqi Zhang. Foundation Models for Weather and Climate Data Understanding: A Comprehensive Survey, 2023. 2
- [21] Yinbo Chen, Rohit Girdhar, Xiaolong Wang, Sai Saketh Rambhatla, and Ishan Misra. Diffusion Autoencoders are Scalable Image Tokenizers, 2025. 3, 4, 6
- [22] P. Cheung and H.Y. Yeung. Application of optical-flow technique to significant convection nowcast for terminal areas in Hong Kong. In *The 3rd WMO International Symposium on Nowcasting and Very Short-Range Forecastin*, Rio de Janeiro, Brazil, 2012. WMO. 2, 10
- [23] Brian Collins, Yunru Lai, Uwe Grewer, Steve Attard, Justin Sexton, and Keith G. Pembleton. Evaluating the impact of weather forecasts on productivity and environmental footprint of irrigated maize production systems. *Science of The Total Environment*, 954:176368, 2024. 1
- [24] Katherine Crowson, Stefan Andreas Baumann, Alex Birch, Tanishq Mathew Abraham, Daniel Z. Kaplan, and Enrico Shippole. Scalable High-Resolution Pixel-Space Image Synthesis with Hourglass Diffusion Transformers. In *Proceedings of the 41st International Conference on Machine Learning*, pages 9550–9575. PMLR, 2024. 2, 4, 7
- [25] Saurabh Das, Animesh Maitra, and Ashish K. Shukla. Rain Attenuation Modeling in the 10-100 GHz Frequency using Drop Size Distributions for different Climatic Zones in Tropical India. *Progress In Electromagnetics Research B*, 25:211–224, 2010. 2
- [26] Luca Delle Monache, Joshua P. Hacker, Yongmei Zhou, Xingxiu Deng, and Roland B. Stull. Probabilistic aspects of meteorological and ozone regional ensemble forecasts. *Journal of Geophysical Research: Atmospheres*, 111(D24): 2005JD006917, 2006. 7
- [27] Laurent Dinh, Jascha Sohl-Dickstein, and Samy Bengio. Density estimation using real nvp. In *International Conference on Learning Representations*, 2017. 3
- [28] Alexey Dosovitskiy, Lucas Beyer, Alexander Kolesnikov, Dirk Weissenborn, Xiaohua Zhai, Thomas Unterthiner, Mostafa Dehghani, Matthias Minderer, G Heigold, S Gelly, et al. An image is worth 16x16 words: Transformers for image recognition at scale. In *ICLR*, 2020. 7, 10
- [29] David C. Dowell, Curtis R. Alexander, Eric P. James, Stephen S. Weygandt, Stanley G. Benjamin, Geoffrey S. Manikin, Benjamin T. Blake, John M. Brown, Joseph B. Olson, Ming Hu, Tatiana G. Smirnova, Terra Ladwig, Jaymes S. Kenyon, Ravan Ahmadov, David D. Turner, Jeffrey D. Duda, and Trevor I. Alcott. The High-Resolution Rapid Refresh (HRRR): An Hourly Updating Convection-Allowing Forecast Model. Part I: Motivation and System Description. *Weather and Forecasting*, 37(8):1371–1395, 2022. 10, 12
- [30] Gabriele Enea, Tom Reynolds, Mark Weber, Ramon Dalmau Codina, and Dirk Schaefer. Analysis of weather-driven air traffic management challenges for major us and european airports. In *SESAR Innovation Days*, Rome, 2024. SESAR Joint Undertaking. 1
- [31] Lasse Espeholt, Shreya Agrawal, Casper Sønderby, Manoj Kumar, Jonathan Heek, Carla Bromberg, Cenk Gazen, Rob Carver, Marcin Andrychowicz, Jason Hickey, et al. Deep learning for twelve hour precipitation forecasts. *Nature communications*, 13(1):5145, 2022. 1, 10
- [32] Patrick Esser, Sumith Kulal, Andreas Blattmann, Rahim Entezari, Jonas Müller, Harry Saini, Yam Levi, Dominik Lorenz, Axel Sauer, Frederic Boesel, et al. Scaling rectified flow transformers for high-resolution image synthesis. In *ICML*, 2024. 3
- [33] Jesús García Fernández and Siamak Mehrkanoon. Broadunet: Multi-scale feature learning for nowcasting tasks. *Neural Networks*, 144:419–427, 2021. 1, 10
- [34] Yarin Gal and Zoubin Ghahramani. Dropout as a Bayesian Approximation: Representing Model Uncertainty in Deep Learning, 2016. arXiv:1506.02142. 3
- [35] Zhihan Gao, Xingjian Shi, Hao Wang, Yi Zhu, Yuyang Bernie Wang, Mu Li, and Dit-Yan Yeung. Earthformer: Exploring space-time transformers for earth system forecasting. *Advances in Neural Information Processing Systems*, 35:25390–25403, 2022. 2, 3, 6, 7, 8, 10, 11, 12, 21, 22
- [36] Zhangyang Gao, Cheng Tan, Lirong Wu, and Stan Z Li. Simvp: Simpler yet better video prediction. In *Proceedings of the IEEE/CVF Conference on Computer Vision and Pattern Recognition*, pages 3170–3180, 2022. 2, 7, 10, 12
- [37] Zhihan Gao, Xingjian Shi, Boran Han, Hao Wang, Xiaoyong Jin, Danielle Maddix, Yi Zhu, Mu Li, and Yuyang (Bernie) Wang. Prediff: Precipitation nowcasting with latent diffusion models. In *Advances in Neural Information Processing Systems*, pages 78621–78656. Curran Associates, Inc., 2023. 1, 2, 3, 7, 10, 11, 12
- [38] Songwei Ge, Seungjun Nah, Guilin Liu, Tyler Poon, Andrew Tao, Bryan Catanzaro, David Jacobs, Jia-Bin Huang, Ming-Yu Liu, and Yogesh Balaji. Preserve Your Own Correlation: A Noise Prior for Video Diffusion Models. In *2023 IEEE/CVF International Conference on Computer Vision (ICCV)*, pages 22873–22884, Paris, France, 2023. IEEE. 3
- [39] Urs Germann and Isztar Zawadzki. Scale-Dependence of the Predictability of Precipitation from Continental Radar Images. Part I: Description of the Methodology. *Monthly Weather Review*, 130(12):2859–2873, 2002. 2, 10
- [40] Junchao Gong, Lei Bai, Peng Ye, Wanghan Xu, Na Liu, Jianhua Dai, Xiaokang Yang, and Wanli Ouyang. CasCast: Skillful high-resolution precipitation nowcasting via cascaded modelling. In *Proceedings of the 41st International Conference on Machine Learning*, pages 15809–15822, Vienna, Austria, 2024. JMLR.org. 1, 2, 4, 6, 7, 8, 3, 5, 10, 12, 16, 17, 21, 22
- [41] Ian Goodfellow, Jean Pouget-Abadie, Mehdi Mirza, Bing Xu, David Warde-Farley, Sherjil Ozair, Aaron Courville,

- and Yoshua Bengio. Generative adversarial nets. In *Advances in Neural Information Processing Systems*. Curran Associates, Inc., 2014. 1, 2, 11
- [42] Vincent Le Guen and Nicolas Thome. Disentangling physical dynamics from unknown factors for unsupervised video prediction. In *Proceedings of the IEEE/CVF Conference on Computer Vision and Pattern Recognition*, pages 11474–11484, 2020. 2, 7, 10, 11, 12
- [43] Ming Gui, Johannes Schusterbauer, Timy Phan, Felix Krause, Josh Susskind, Miguel Angel Bautista, and Björn Ommer. Adapting self-supervised representations as a latent space for efficient generation, 2025. 2, 4, 5
- [44] William Harvey, Saeid Naderiparizi, Vaden Masrani, Christian Weilbach, and Frank Wood. Flexible diffusion modeling of long videos. *arXiv preprint arXiv:2205.11495*, 2022. 4
- [45] Ali Hassani, Steven Walton, Jiachen Li, Shen Li, and Humphrey Shi. Neighborhood Attention Transformer. In *Proceedings of the IEEE/CVF Conference on Computer Vision and Pattern Recognition*, pages 6185–6194, 2023. 4, 7
- [46] Yingqing He, Tianyu Yang, Yong Zhang, Ying Shan, and Qifeng Chen. Latent Video Diffusion Models for High-Fidelity Long Video Generation, 2023. 3
- [47] Byeongho Heo, Song Park, Dongyoon Han, and Sangdoon Yun. Rotary Position Embedding for Vision Transformer, 2024. 7
- [48] Jonathan Ho and Tim Salimans. Classifier-Free Diffusion Guidance, 2022. 6, 7, 3, 4, 5, 9, 11, 14, 15, 16, 17
- [49] Jonathan Ho, Nal Kalchbrenner, Dirk Weissenborn, and Tim Salimans. Axial Attention in Multidimensional Transformers, 2019. 10
- [50] Jonathan Ho, Ajay Jain, and Pieter Abbeel. Denoising diffusion probabilistic models. *Advances in Neural Information Processing Systems*, 33:6840–6851, 2020. 1, 3, 11
- [51] Sepp Hochreiter and Jürgen Schmidhuber. Long Short-Term Memory. *Neural Comput.*, 9(8):1735–1780, 1997. 10
- [52] Yang Hong, Kuo-Lin Hsu, Soroosh Sorooshian, and Xiaogang Gao. Precipitation Estimation from Remotely Sensed Imagery Using an Artificial Neural Network Cloud Classification System. *Journal of Applied Meteorology and Climatology*, 43(12):1834–1853, 2004. 9
- [53] Yang Hong, Kuo-lin Hsu, Hamid Moradkhani, and Soroosh Sorooshian. Uncertainty quantification of satellite precipitation estimation and Monte Carlo assessment of the error propagation into hydrologic response. *Water Resources Research*, 42(8), 2006. 3
- [54] Tobias Höppe, Arash Mehrjou, Stefan Bauer, Didrik Nielsen, and Andrea Dittadi. Diffusion models for video prediction and infilling. *arXiv preprint arXiv:2206.07696*, 2022. 2, 5, 6, 4
- [55] Shengding Hu, Yuge Tu, Xu Han, Chaoqun He, Ganqu Cui, Xiang Long, Zhi Zheng, Yewei Fang, Yuxiang Huang, Weilin Zhao, Xinrong Zhang, Zheng Leng Thai, Kaihuo Zhang, Chongyi Wang, Yuan Yao, Chenyang Zhao, Jie Zhou, Jie Cai, Zhongwu Zhai, Ning Ding, Chao Jia, Guoyang Zeng, Dahai Li, Zhiyuan Liu, and Maosong Sun. MiniCPM: Unveiling the Potential of Small Language Models with Scalable Training Strategies, 2024. 7
- [56] Drew A. Hudson, Daniel Zoran, Mateusz Malinowski, Andrew K. Lampinen, Andrew Jaegle, James L. McClelland, Loic Matthey, Felix Hill, and Alexander Lerchner. SODA: Bottleneck Diffusion Models for Representation Learning. In *Proceedings of the IEEE/CVF Conference on Computer Vision and Pattern Recognition*, pages 23115–23127, 2024. 3
- [57] Eyke Hüllermeier and Willem Waegeman. Aleatoric and epistemic uncertainty in machine learning: An introduction to concepts and methods. *Machine Learning*, 110(3):457–506, 2021. 3, 11
- [58] Junhwa Hur and Stefan Roth. Iterative Residual Refinement for Joint Optical Flow and Occlusion Estimation, 2019. 2
- [59] Ruben O. Imhoff, Lesley De Cruz, Wout Dewettinck, Claudia C. Brauer, Remko Uijlenhoet, Klaas-Jan Van Heeringen, Carlos Velasco-Forero, Daniele Nerini, Michiel Van Ginderachter, and Albrecht H. Weerts. Scale-dependent blending of ensemble rainfall nowcasts and numerical weather prediction in the open-source pysteps library. *Quarterly Journal of the Royal Meteorological Society*, 149(753):1335–1364, 2023. 11
- [60] Japan Meteorological Agency. Users’ guide to imagery with heavy rainfall potential areas, 2014. 9
- [61] Yan Ji, Bing Gong, Michael Langguth, Amirpasha Mozafari, and Xiefei Zhi. Clgan: A gan-based video prediction model for precipitation nowcasting. *EGU Sphere*, pages 1–23, 2022. 11
- [62] Wenjun Jiang, Xi Zhong, and Jize Zhang. TC-Diffusion: A diffusion-based probabilistic tropical cyclone model with application to typhoon wind hazard assessment. *Reliability Engineering & System Safety*, 251:110350, 2024. 2
- [63] John D. Kanellopoulos, Stelios G. Koukoulas, Nicolaos J. Kolliopoulos, Christos N. Capsalis, and Spyros G. Ventouras. Rain attenuation problems affecting the performance of microwave communication systems. *Annales des Télécommunications*, 45(7):437–451, 1990. 2
- [64] Hassan K. Khalil. *Nonlinear Systems*. Prentice Hall, Upper Saddle River, NJ, 3. ed edition, 2002. 10
- [65] Diederik P. Kingma and Max Welling. Auto-encoding variational bayes. In *2nd International Conference on Learning Representations, ICLR 2014, Banff, AB, Canada, April 14-16, 2014, Conference Track Proceedings*, 2014. 2
- [66] Youssef Kossale, Mohammed Airaj, and Aziz Darouichi. Mode Collapse in Generative Adversarial Networks: An Overview. In *2022 8th International Conference on Optimization and Applications (ICOA)*, pages 1–6, 2022. 1, 2, 4, 11
- [67] Balaji Lakshminarayanan, Alexander Pritzel, and Charles Blundell. Simple and scalable predictive uncertainty estimation using deep ensembles. In *Proceedings of the 31st International Conference on Neural Information Processing Systems*, pages 6405–6416, Red Hook, NY, USA, 2017. Curran Associates Inc. 3
- [68] Remi Lam, Alvaro Sanchez-Gonzalez, Matthew Willson, Peter Wirnsberger, Meire Fortunato, Ferran Alet, Suman

- Ravuri, Timo Ewalds, Zach Eaton-Rosen, Weihua Hu, Alexander Merose, Stephan Hoyer, George Holland, Oriol Vinyals, Jacklynn Stott, Alexander Pritzel, Shakir Mohamed, and Peter Battaglia. Learning skillful medium-range global weather forecasting. *Science*, 2023. 11
- [69] Lev Davidovich Landau and Evgenii Mikhailovich Lifshits. *Fluid Mechanics*. Number v. 6 in *Their Course of Theoretical Physics*. Pergamon Press, London, 1959. 10
- [70] Gwennaëlle Larvor, Léa Berthomier, Vincent Chabot, Brice Le Pape, Bruno Pradel, and Lior Perez. Meteonet, an open reference weather dataset by meteo-france. *URL https://meteonet.umr-cnrm.fr/*, 2020. 6, 3
- [71] Jussi Leinonen, Ulrich Hamann, Daniele Nerini, Urs Germann, and Gabriele Franch. Latent diffusion models for generative precipitation nowcasting with accurate uncertainty quantification. *arXiv preprint arXiv:2304.12891*, 2023. 1, 2, 3, 4, 7, 10, 11, 12
- [72] Lizao Li, Rob Carver, Ignacio Lopez-Gomez, Fei Sha, and John Anderson. SEEDS: Emulation of Weather Forecast Ensembles with Diffusion Models, 2023. 12
- [73] Lizao Li, Robert Carver, Ignacio Lopez-Gomez, Fei Sha, and John Anderson. Generative emulation of weather forecast ensembles with diffusion models. *Science Advances*, 10(13):eadk4489, 2024. 7
- [74] Weidong Li, Baoxiang Pan, Tiejian Li, Congyi Nai, Zhaoxi Li, Bo Lu, Qingyun Duan, and Ming Pan. Latent Diffusion Model for Quantitative Precipitation Estimation and Forecast at km Scale. *ESS Open Archive*, 2024. 2, 10, 11, 12
- [75] Zongjian Li, Bin Lin, Yang Ye, Liuhan Chen, Xinhua Cheng, Shenghai Yuan, and Li Yuan. WF-VAE: Enhancing Video VAE by Wavelet-Driven Energy Flow for Latent Video Diffusion Model, 2025. 2, 3
- [76] Soon Hoe Lim, Yijin Wang, Annan Yu, Emma Hart, Michael W. Mahoney, Xiaoye S. Li, and N. Benjamin Erichson. Elucidating the design choice of probability paths in flow matching for forecasting, 2024. 9
- [77] Xudong Ling, Chaorong Li, Fengqing Qin, Peng Yang, and Yuanyuan Huang. SRNDiff: Short-term Rainfall Nowcasting with Condition Diffusion Model, 2024. 2, 4, 11, 12
- [78] Yaron Lipman, Ricky TQ Chen, Heli Ben-Hamu, Maximilian Nickel, and Matthew Le. Flow matching for generative modeling. In *ICLR*, 2023. 1, 3
- [79] Hong-Bin Liu and Ickjai Lee. MPL-GAN: Toward Realistic Meteorological Predictive Learning Using Conditional GAN. *IEEE Access*, 8:93179–93186, 2020. 1, 2, 11
- [80] Xingchao Liu, Chengyue Gong, and Qiang Liu. Flow Straight and Fast: Learning to Generate and Transfer Data with Rectified Flow, 2022. 1, 3
- [81] Edward N. Lorenz. Deterministic Nonperiodic Flow. *Journal of the Atmospheric Sciences*, 20(2):130–141, 1963. 10
- [82] Ilya Loshchilov and Frank Hutter. Decoupled Weight Decay Regularization, 2019. 7
- [83] Zhengxiong Luo, Dayou Chen, Yingya Zhang, Yan Huang, Liang Wang, Yujun Shen, Deli Zhao, Jingren Zhou, and Tieniu Tan. Videofusion: Decomposed diffusion models for high-quality video generation. In *Proceedings of the IEEE/CVF Conference on Computer Vision and Pattern Recognition*, pages 10209–10218, 2023. 3
- [84] Nanye Ma, Mark Goldstein, Michael S. Albergo, Nicholas M. Boffi, Eric Vanden-Eijnden, and Saining Xie. SiT: Exploring Flow and Diffusion-based Generative Models with Scalable Interpolant Transformers, 2024. 2, 3, 7
- [85] David J. C. MacKay. *Bayesian methods for adaptive models*. phd, California Institute of Technology, 1992. 3
- [86] David J. C. MacKay. A Practical Bayesian Framework for Backpropagation Networks. *Neural Computation*, 4(3): 448–472, 1992. 3
- [87] J. Milford, V. D. McDougall, and G. Dugdale. Rainfall estimation from cold cloud duration : Experience of the TAM-SAT group in West Africa. In *Validation Des Methodes D'estimation Des Precipitations Par Satellite*, 1996. 9
- [88] Mehdi Mirza and Simon Osindero. Conditional Generative Adversarial Nets, 2014. 11
- [89] F. Molteni, R. Buizza, T. N. Palmer, and T. Petroliagis. The ecmwf ensemble prediction system: Methodology and validation. *Quarterly Journal of the Royal Meteorological Society*, 122(529):73–119, 1996. 10, 11
- [90] Congyi Nai, Baoxiang Pan, Xi Chen, QiuHong Tang, Guangheng Ni, Qingyun Duan, Bo Lu, Ziniu Xiao, and Xingcai Liu. Reliable precipitation nowcasting using probabilistic diffusion models. *Environmental Research Letters*, 19(3):034039, 2024. 2, 3, 4, 11
- [91] Claude-Louis-Marie-Henri Navier. *Mémoire sur les lois du mouvement des fluides*. l'Académie Royale des Sciences de l'Institut de France, 1827. 10
- [92] Tung Nguyen, Johannes Brandstetter, Ashish Kapoor, Jayesh K Gupta, and Aditya Grover. Climax: A foundation model for weather and climate. *arXiv preprint arXiv:2301.10343*, 2023. 11
- [93] Alexander Quinn Nichol and Prafulla Dhariwal. Improved denoising diffusion probabilistic models. In *International Conference on Machine Learning*, pages 8162–8171. PMLR, 2021. 3, 11
- [94] NOAA / National Centers For Environmental Information. NOAA Storm Events Database, 2020. 7
- [95] Juan Nunez-Portillo, Alfonso Valenzuela, Antonio Franco, and Damián Rivas. Predicting air traffic congestion under uncertain adverse weather. *Aerospace*, 11(3):240, 2024. 1
- [96] Edward Ott. *Chaos in Dynamical Systems*. Cambridge Univ. Press, Cambridge, repr edition, 2000. 10
- [97] Jaideep Pathak, Shashank Subramanian, Peter Harrington, Sanjeev Raja, Ashesh Chattopadhyay, Morteza Mardani, Thorsten Kurth, David Hall, Zongyi Li, Kamyar Azizzadenesheli, Pedram Hassanzadeh, Karthik Kashinath, and Animeshree Anandkumar. FourCastNet: A Global Data-driven High-resolution Weather Model using Adaptive Fourier Neural Operators, 2022. 2, 10, 11
- [98] Jaideep Pathak, Yair Cohen, Piyush Gard, Peter Harrington, Noah Brenowitz, Dale Durran, Morteza Mardani, Arash Vahdat, Shaoming Xu, Karthik Kashinath, and Mike Pritchard. Kilometer-Scale Convection Allowing Model Emulation using Generative Diffusion Modeling, 2024. 2, 3, 12
- [99] William Peebles and Saining Xie. Scalable Diffusion Models with Transformers, 2023. 2, 7, 12

- [100] Jordan G. Powers, Joseph B. Klemp, William C. Skamarock, Christopher A. Davis, Jimy Dudhia, David O. Gill, Janice L. Coen, David J. Gochis, Ravan Ahmadov, Steven E. Peckham, Georg A. Grell, John Michalakes, Samuel Trahan, Stanley G. Benjamin, Curtis R. Alexander, Geoffrey J. Dimego, Wei Wang, Craig S. Schwartz, Glen S. Romine, Zhiqun Liu, Chris Snyder, Fei Chen, Michael J. Barlage, Wei Yu, and Michael G. Duda. The Weather Research and Forecasting Model: Overview, System Efforts, and Future Directions. *Bulletin of the American Meteorological Society*, 98(8):1717–1737, 2017. 11
- [101] Konpat Preechakul, Nattanat Chatthee, Suttisak Wizadwongsa, and Supasorn Suwajanakorn. Diffusion Autoencoders: Toward a Meaningful and Decodable Representation. In *Proceedings of the IEEE/CVF Conference on Computer Vision and Pattern Recognition*, pages 10619–10629, 2022. 3
- [102] Ilan Price and Stephan Rasp. Increasing the accuracy and resolution of precipitation forecasts using deep generative models. In *International conference on artificial intelligence and statistics*, pages 10555–10571. PMLR, 2022. 11
- [103] Ilan Price, Alvaro Sanchez-Gonzalez, Ferran Alet, Tom R. Andersson, Andrew El-Kadi, Dominic Masters, Timo Ewalds, Jacklynn Stott, Shakir Mohamed, Peter Battaglia, Remi Lam, and Matthew Willson. GenCast: Diffusion-based ensemble forecasting for medium-range weather, 2024. 2, 11
- [104] Seppo Pulkkinen, Daniele Nerini, Andrés A Pérez Hortal, Carlos Velasco-Forero, Alan Seed, Urs Germann, and Loris Foresti. Pysteps: an open-source python library for probabilistic precipitation nowcasting (v1.0). *Geoscientific Model Development*, 12(10):4185–4219, 2019. 11
- [105] Francisco Raimundo, André Glória, and Pedro Sebastião. Prediction of weather forecast for smart agriculture supported by machine learning. In *2021 IEEE World AI IoT Congress (AllIoT)*, pages 0160–0164, 2021. 1
- [106] Azizul Azhar Ramli, Mohammad Rabiul Islam, Mohd Farhan Md. Fudzee, Mohamad Aizi Salamat, and Shahreen Kasim. A practical weather forecasting for air traffic control system using fuzzy hierarchical technique. In *Recent Advances on Soft Computing and Data Mining*, pages 99–109, Cham, 2014. Springer International Publishing. 1
- [107] Suman Ravuri, Karel Lenc, Matthew Willson, Dmitry Kangin, Remi Lam, Piotr Mirowski, Megan Fitzsimons, Maria Athanassiadou, Sheleem Kashem, Sam Madge, et al. Skilful precipitation nowcasting using deep generative models of radar. *Nature*, 597(7878):672–677, 2021. 1, 2, 11
- [108] Brett Roberts, Burkely T. Gallo, Israel L. Jirak, and Adam J. Clark. The High Resolution Ensemble Forecast (HREF) system: Applications and Performance for Forecasting Convective Storms. *Authorea*, 2025. 10
- [109] Christopher D. Roberts, Retish Senan, Franco Molteni, Souhail Boussetta, Michael Mayer, and Sarah P. E. Keeley. Climate model configurations of the ECMWF Integrated Forecasting System (ECMWF-IFS cycle 43r1) for High-ResMIP. *Geoscientific Model Development*, 11(9):3681–3712, 2018. 10
- [110] Robin Rombach, Andreas Blattmann, Dominik Lorenz, Patrick Esser, and Björn Ommer. High-resolution image synthesis with latent diffusion models. In *Proceedings of the IEEE/CVF conference on computer vision and pattern recognition*, pages 10684–10695, 2022. 1, 2, 3, 4, 5, 11
- [111] Olaf Ronneberger, Philipp Fischer, and Thomas Brox. U-Net: Convolutional Networks for Biomedical Image Segmentation. In *Medical Image Computing and Computer-Assisted Intervention – MICCAI 2015*, pages 234–241. Springer International Publishing, Cham, 2015. 10
- [112] Seyedmorteza Sadat, Otmar Hilliges, and Romann M. Weber. Eliminating Oversaturation and Artifacts of High Guidance Scales in Diffusion Models, 2024. 3, 4
- [113] Mojtaba Sadeghi, Ata Akbari Asanjan, Mohammad Faridzad, Phu Nguyen, Kuolin Hsu, Soroosh Sorooshian, and Dan Braithwaite. PERSIANN-CNN: Precipitation Estimation from Remotely Sensed Information Using Artificial Neural Networks–Convolutional Neural Networks. *Journal of Hydrometeorology*, 20(12):2273–2289, 2019. 9
- [114] Hidetomo Sakaino. Spatio-Temporal Image Pattern Prediction Method Based on a Physical Model With Time-Varying Optical Flow. *IEEE Transactions on Geoscience and Remote Sensing*, 51(5):3023–3036, 2013. 2, 10
- [115] Lei She, Chenghong Zhang, Xin Man, and Jie Shao. LLMDiff: Diffusion model using frozen llm transformers for precipitation nowcasting. *Sensors*, 24(18):6049, 2024. 8, 11
- [116] Danna Shen, Xiaofeng Zhao, Leyi Chai, Zhuanzhuan Guo, and Chunxiang Leng. Analysis of the agricultural economic value of a weather forecasting service based on a survey of peasant households in chinese provinces. *Humanities and Social Sciences Communications*, 11(1):1–7, 2024. 1
- [117] Jie Shi, Chenfei Wu, Jian Liang, Xiang Liu, and Nan Duan. DiVAE: Photorealistic Images Synthesis with Denoising Diffusion Decoder, 2022. 3
- [118] Jimeng Shi, Bowen Jin, Jiawei Han, and Giri Narasimhan. CoDiCast: Conditional Diffusion Model for Weather Prediction with Uncertainty Quantification, 2024. 3, 4, 11, 12
- [119] Wenzhe Shi, Jose Caballero, Ferenc Huszar, Johannes Totz, Andrew P. Aitken, Rob Bishop, Daniel Rueckert, and Zehan Wang. Real-Time Single Image and Video Super-Resolution Using an Efficient Sub-Pixel Convolutional Neural Network. In *2016 IEEE Conference on Computer Vision and Pattern Recognition (CVPR)*, pages 1874–1883, Las Vegas, NV, USA, 2016. IEEE. 4, 7
- [120] Xingjian Shi, Zhoung Chen, Hao Wang, Dit-Yan Yeung, Wai-Kin Wong, and Wang-chun Woo. Convolutional lstm network: A machine learning approach for precipitation nowcasting. *Advances in neural information processing systems*, 28, 2015. 2, 7, 10, 11, 12
- [121] Xingjian Shi, Zhihan Gao, Leonard Lausen, Hao Wang, Dit-Yan Yeung, Wai-kin Wong, and Wang-chun Woo. Deep learning for precipitation nowcasting: A benchmark and a new model. *Advances in neural information processing systems*, 30, 2017. 2, 10
- [122] Dule Shu and Amir Barati Farimani. Zero-Shot Uncertainty Quantification using Diffusion Probabilistic Models, 2024. 1, 3

- [123] Uriel Singer, Adam Polyak, Thomas Hayes, Xi Yin, Jie An, Songyang Zhang, Qiyuan Hu, Harry Yang, Oron Ashual, Oran Gafni, Devi Parikh, Sonal Gupta, and Yaniv Taigman. Make-A-Video: Text-to-Video Generation without Text-Video Data, 2022. 3
- [124] Jascha Sohl-Dickstein, Eric Weiss, Niru Maheswaranathan, and Surya Ganguli. Deep unsupervised learning using nonequilibrium thermodynamics. In *International Conference on Machine Learning*, pages 2256–2265. PMLR, 2015. 11
- [125] Casper Kaae Sønderby, Lasse Espeholt, Jonathan Heek, Mostafa Dehghani, Avital Oliver, Tim Salimans, Shreya Agrawal, Jason Hickey, and Nal Kalchbrenner. Metnet: A neural weather model for precipitation forecasting. *arXiv preprint arXiv:2003.12140*, 2020. 2, 10, 11
- [126] Jiaming Song, Chenlin Meng, and Stefano Ermon. Denoising diffusion implicit models. *arXiv preprint arXiv:2010.02502*, 2020. 1, 3
- [127] Yang Song and Stefano Ermon. Generative modeling by estimating gradients of the data distribution. *Advances in neural information processing systems*, 32, 2019. 1, 3
- [128] Simone Sperati, Stefano Alessandrini, and Luca Delle Monache. An application of the ECMWF Ensemble Prediction System for short-term solar power forecasting. *Solar Energy*, 133:437–450, 2016. 1
- [129] Nitish Srivastava, Geoffrey Hinton, Alex Krizhevsky, Ilya Sutskever, and Ruslan Salakhutdinov. Dropout: A Simple Way to Prevent Neural Networks from Overfitting. *Journal of Machine Learning Research*, 15(56):1929–1958, 2014. 3
- [130] Jason Stock, Jaideep Pathak, Yair Cohen, Mike Pritchard, Piyush Garg, Dale Durran, Morteza Mardani, and Noah D. Brenowitz. DiffObs: Generative Diffusion for Global Forecasting of Satellite Observations. In *Climate Change AI. Climate Change AI*, 2024. 11
- [131] G. G. Stokes. On the Theories of the Internal Friction of Fluids in Motion, and of the Equilibrium and Motion of Elastic Solids. In *Classics of Elastic Wave Theory*, page 0. Society of Exploration Geophysicists, 2007. 10
- [132] Jianlin Su, Yu Lu, Shengfeng Pan, Ahmed Murtafha, Bo Wen, and Yunfeng Liu. RoFormer: Enhanced Transformer with Rotary Position Embedding, 2023. 7
- [133] Anni Tang, Tianyu He, Junliang Guo, Xinle Cheng, Li Song, and Jiang Bian. VidTok: A Versatile and Open-Source Video Tokenizer, 2024. 2, 3
- [134] The European Space Agency. Types of orbits. https://www.esa.int/Enabling_Support/Space_Transportation, 2020. 9
- [135] The Movie Gen team @ Meta. Movie Gen: A Cast of Media Foundation Models, 2024. 3, 4, 5, 7
- [136] Kevin Trebing, Tomasz Stanczyk, and Siamak Mehrkanoon. Smaat-unet: Precipitation nowcasting using a small attention-unet architecture. *Pattern Recognition Letters*, 145:178–186, 2021. 1, 10
- [137] Matias Valdenegro-Toro and Daniel Saromo Mori. A Deeper Look into Aleatoric and Epistemic Uncertainty Disentanglement. In *2022 IEEE/CVF Conference on Computer Vision and Pattern Recognition Workshops (CVPRW)*, pages 1508–1516, 2022. ISSN: 2160-7516. 3
- [138] Ashish Vaswani, Noam Shazeer, Niki Parmar, Jakob Uszkoreit, Llion Jones, Aidan N Gomez, Łukasz Kaiser, and Illia Polosukhin. Attention is All you Need. In *Advances in Neural Information Processing Systems*. Curran Associates, Inc., 2017. 10
- [139] Mark Veillette, Siddharth Samsi, and Chris Mattioli. SE-VIR : A Storm Event Imagery Dataset for Deep Learning Applications in Radar and Satellite Meteorology. In *Advances in Neural Information Processing Systems*, pages 2209–22019. Curran Associates, Inc., 2020. 2, 6, 3, 7, 8
- [140] Yogesh Verma, Markus Heinonen, and Vikas Garg. ClimODE: Climate and Weather Forecasting with Physics-informed Neural ODEs, 2024. arXiv:2404.10024. 11
- [141] Huai-zhi Wang, Gang-qiang Li, Gui-bin Wang, Jian-chun Peng, Hui Jiang, and Yi-tao Liu. Deep learning based ensemble approach for probabilistic wind power forecasting. *Applied Energy*, 188:56–70, 2017. 1
- [142] Junke Wang, Yi Jiang, Zehuan Yuan, Binyue Peng, Zuxuan Wu, and Yu-Gang Jiang. OmniTokenizer: A Joint Image-Video Tokenizer for Visual Generation. *Advances in Neural Information Processing Systems*, 37:28281–28295, 2024. 2, 3
- [143] Wenjing Wang, Huan Yang, Zixi Tuo, Huiguo He, Junchen Zhu, Jianlong Fu, and Jiaying Liu. Swap Attention in Spatiotemporal Diffusions for Text-to-Video Generation, 2024. 3
- [144] Yunbo Wang, Mingsheng Long, Jianmin Wang, Zhifeng Gao, and Philip S Yu. Predrnn: Recurrent neural networks for predictive learning using spatiotemporal lstms. *Advances in neural information processing systems*, 30, 2017. 2, 7, 10, 11
- [145] D. S. Wilks. Indices of Rank Histogram Flatness and Their Sampling Properties. *Monthly Weather Review*, 147(2): 763–769, 2019. 7
- [146] Wang-Chun Woo. Application of Optical Flow Techniques to Rainfall Nowcasting. In *27th Conference on Severe Local Storms*. AMS, 2014. 2, 10
- [147] Wang-chun Woo and Wai-kin Wong. Operational Application of Optical Flow Techniques to Radar-Based Rainfall Nowcasting. *Atmosphere*, 8(3):48, 2017. 2, 10
- [148] Yuan-Kang Wu, Po-En Su, Ting-Yi Wu, Jing-Shan Hong, and Mohammad Yusri Hassan. Probabilistic Wind-Power Forecasting Using Weather Ensemble Models. *IEEE Transactions on Industry Applications*, 54(6):5609–5620, 2018. 1
- [149] Yazhou Xing, Yang Fei, Yingqing He, Jingye Chen, Jiaxin Xie, Xiaowei Chi, and Qifeng Chen. Large motion video autoencoding with cross-modal video vae, 2024. 2, 3
- [150] Nianzu Yang, Pandeng Li, Liming Zhao, Yang Li, Chen-Wei Xie, Yehui Tang, Xudong Lu, Zhihang Liu, Yun Zheng, Yu Liu, and Junchi Yan. Rethinking Video Tokenization: A Conditioned Diffusion-based Approach, 2025. 2, 3, 4, 6
- [151] Yimin Yang and Siamak Mehrkanoon. Aa-transunet: Attention augmented transunet for nowcasting tasks. In *2022 International Joint Conference on Neural Networks (IJCNN)*, pages 01–08. IEEE, 2022. 10

- [152] Jingfeng Yao, Bin Yang, and Xinggang Wang. Reconstruction vs. generation: Taming optimization dilemma in latent diffusion models. In *Proceedings of the IEEE/CVF Conference on Computer Vision and Pattern Recognition*, 2025. [5](#)
- [153] Demin Yu, Xutao Li, Yunming Ye, Baoquan Zhang, Chuyao Luo, Kuai Dai, Rui Wang, and Xunlai Chen. Diff-Cast: A Unified Framework via Residual Diffusion for Precipitation Nowcasting. In *Proceedings of the IEEE/CVF Conference on Computer Vision and Pattern Recognition*, pages 27758–27767, 2024. [2](#), [3](#), [7](#), [9](#), [12](#)
- [154] Lijun Yu, Jose Lezama, Nitesh Bharadwaj Gundavarapu, Luca Versari, Kihyuk Sohn, David Minnen, Yong Cheng, Agrim Gupta, Xiuye Gu, Alexander G. Hauptmann, Boqing Gong, Ming-Hsuan Yang, Irfan Essa, David A. Ross, and Lu Jiang. Language Model Beats Diffusion - Tokenizer is key to visual generation. In *The Twelfth International Conference on Learning Representations*, 2023. [3](#)
- [155] Qihang Yu, Mark Weber, Xueqing Deng, Xiaohui Shen, Daniel Cremers, and Liang-Chieh Chen. An Image is Worth 32 Tokens for Reconstruction and Generation, 2024. [3](#)
- [156] Seongjun Yun, Minbyul Jeong, Raehyun Kim, Jaewoo Kang, and Hyunwoo J Kim. Graph Transformer Networks. In *Advances in Neural Information Processing Systems*. Curran Associates, Inc., 2019. [11](#)
- [157] Richard Zhang, Phillip Isola, Alexei A Efros, Eli Shechtman, and Oliver Wang. The unreasonable effectiveness of deep features as a perceptual metric. In *CVPR*, 2018. [2](#), [12](#)
- [158] Yuchen Zhang, Mingsheng Long, Kaiyuan Chen, Lanxiang Xing, Ronghua Jin, Michael I Jordan, and Jianmin Wang. Skilful nowcasting of extreme precipitation with nowcastnet. *Nature*, 619(7970):526–532, 2023. [1](#), [2](#), [7](#), [3](#), [11](#)
- [159] Yitian Zhang, Long Mai, Aniruddha Mahapatra, David Bourgin, Yicong Hong, Jonah Casebeer, Feng Liu, and Yun Fu. Regen: Learning compact video embedding with (re-)generative decoder, 2025. [2](#), [3](#), [4](#), [6](#)
- [160] Long Zhao, Sanghyun Woo, Ziyu Wan, Yandong Li, Han Zhang, Boqing Gong, Hartwig Adam, Xuhui Jia, and Ting Liu. Epsilon-VAE: Denoising as Visual Decoding, 2025. [3](#), [4](#), [6](#)
- [161] Boyang Zheng, Nanye Ma, Shengbang Tong, and Saining Xie. Diffusion transformers with representation autoencoders, 2025. [2](#), [4](#), [5](#)
- [162] Xiaqiong Zhou, Yuejian Zhu, Dingchen Hou, Bing Fu, Wei Li, Hong Guan, Eric Sinsky, Walter Kolczynski, Xianwu Xue, Yan Luo, Jiayi Peng, Bo Yang, Vijay Tallapragada, and Philip Pegion. The Development of the NCEP Global Ensemble Forecast System Version 12. *Weather and Forecasting*, 37(6):1069–1084, 2022. [11](#)

Probabilistic Precipitation Nowcasting with Rectified Flow Transformers

Supplementary Material

A. Extended Results

A.1. Extreme Precipitation

We further evaluate our method under extreme weather conditions. We define extreme weather as the top 20% of events with the highest average precipitation, and the rest as “normal”.

Forecasting Performance We provide a quantitative comparison between our method and the state-of-the-art CasCast method [40] in extreme weather in Tab. 6. Under extreme conditions, the CRPS and SSIM deteriorate for all models, indicating that prediction is more difficult in chaotic extreme events. Interestingly, localization-centric metrics improve for all methods. Therefore, determining the movement of extreme patterns seems to be easier than predicting the onset of light to medium rain. Notably, the performance gap for these metrics between our method and CasCast further narrows. Hence, our approach achieves comparable localization performance to state-of-the-art methods in critical extreme weather scenarios while maintaining superior distribution coverage. Furthermore, the scaling properties discussed in Sec. 4.3 hold under extreme conditions. The L-LSM achieves the best CRPS and SSIM scores, and HSS and CSI match the results from CasCast [40] closely with classifier-free guidance. Therefore, our L variant is particularly well-suited to determine localized risk at improved distribution coverage compared to prior methods.

Reconstruction Performance In addition to the regression experiment in Fig. 6 in the main paper, we quantitatively analyze the differences between reconstruction ensemble members for extreme and normal weather in Tab. 7. We find $2.4\times$ higher variance with extreme weather, and intra-ensemble differences, as measured by RMSE, are $1.5\times$ higher for extreme weather. This result confirms that reconstructions of chaotic extreme weather events show larger ensemble differences, indicating higher uncertainty.

Table 6. Comparison of CasCast [40] with our method for extreme weather events. Extreme weather is defined as the 80th percentile of all events with the highest precipitation.

| Model | CRPS↓ | SSIM↑ | HSS↑ | CSI↑ |
|--------------|---------------|---------------|---------------|---------------|
| CasCast [40] | 0.0404 | 0.6354 | 0.5726 | 0.4728 |
| Our B-LSM | 0.0384 | 0.6514 | 0.4982 | 0.4162 |
| ↳ with cfg | 0.0400 | 0.6634 | 0.5321 | 0.4678 |
| Our L-LSM | 0.0357 | 0.6602 | 0.5107 | 0.4233 |
| ↳ with cfg | 0.0360 | 0.6731 | 0.5659 | 0.4677 |

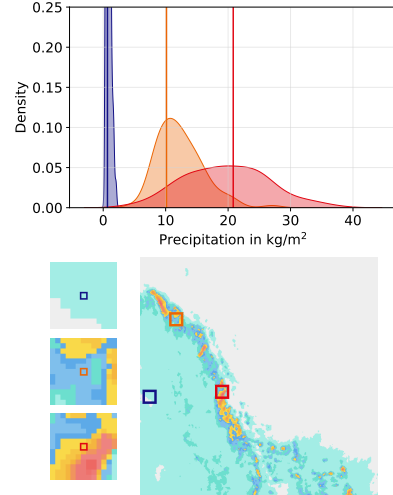


Figure S1. Forecasting ensemble distributions for three pixels of low, medium, and high precipitation regions. Vertical lines show ground truth precipitation. The more extreme the weather, the larger the distribution spread, indicating higher uncertainty.

Table 7. Differences over reconstructions from a 10-member T_{reg} FREUD ensemble. Extreme weather events are defined as the 80th percentile of all events in the validation dataset with the highest average precipitation.

| Weather Data | Var $\times 10^{-5}$ | SD $\times 10^{-3}$ | RMSE $\times 10^{-2}$ | MAE $\times 10^{-3}$ |
|--------------|----------------------|---------------------|-----------------------|----------------------|
| Extreme | 6.866 | 5.066 | 1.172 | 5.737 |
| Normal | 2.849 | 2.003 | 0.769 | 2.884 |

Extreme Weather Phenomena We further assess how well our method generalizes to rare and extreme weather phenomena by evaluating the few labeled severe events in the SEVIR train and test sets. As shown in Tab. 8, our approach consistently outperforms CasCast across tornado, flood, and flash-flood cases, demonstrating clear advantages. Beyond these quantitative results, we show a qualitative example in Fig. S2, which shows that our model can capture the large-scale rotational dynamics and global motion patterns characteristic of a hurricane. We further provide video visualizations that illustrate the circular motion more clearly.

A.2. Ensemble Distributions

Error Distributions Fig. S4 shows the distribution of deviations from ground-truth precipitation, for FREUD and our forecasting model (B-LSM), where 0 denotes a perfect forecast. We only consider pixels where precipitation is ob-

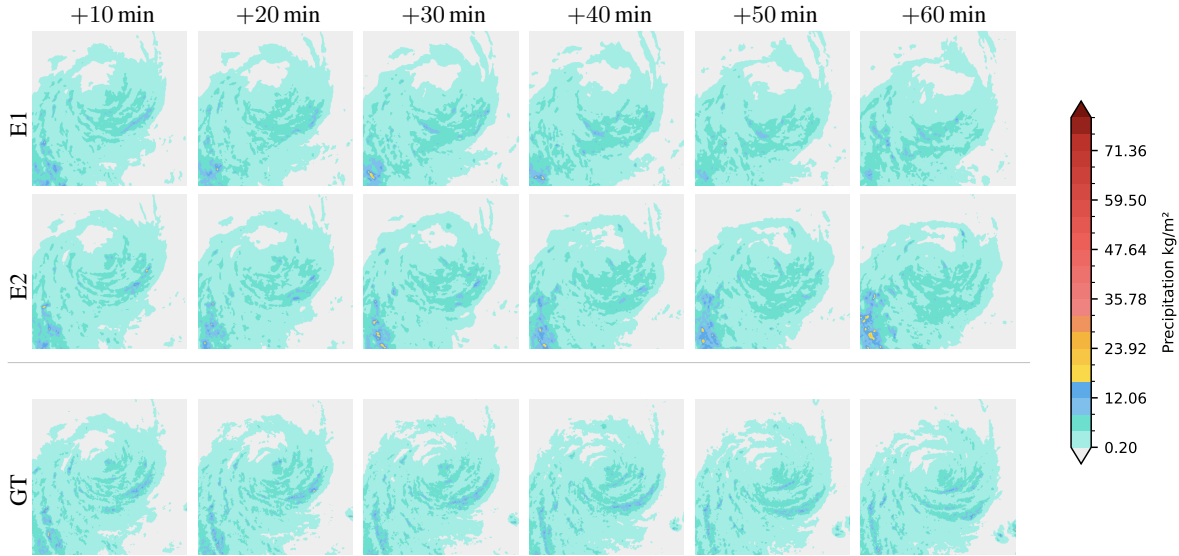


Figure S2. Qualitative sample from a known hurricane event. Our method is able to capture the circular motion observed in the ground truth. For a better visualization of circular motion, please refer to the supplemented video visualizations.

Table 8. Reconstruction and forecasting performance on rare and severe SEVIR weather events. We compare CasCast [40] with our method across reconstruction metrics (RMSE, PSNR, SSIM) and forecasting metrics (CRPS, HSS) for tornado, flood, and flash-flood subsets.

| Event | Model | Reconstruction | | | Forecast | |
|--------------------------|-------------|----------------------|-----------------------|---------------------|-----------------------|-----------------------|
| | | RMSE | PSNR | SSIM | CRPS | HSS |
| Tornado (194 events) | CasCast | 0.104 | 22.800 | 0.957 | 0.0627 | 0.4675 |
| | Ours | 0.0120 -0.092 | 38.434 +15.634 | 0.970 +0.013 | 0.0374 -0.0253 | 0.4882 +0.0207 |
| Flood (177 events) | CasCast | 0.080 | 25.316 | 0.960 | 0.0488 | 0.4493 |
| | Ours | 0.011 -0.069 | 39.236 +13.920 | 0.971 +0.011 | 0.0280 -0.0208 | 0.4106 -0.0387 |
| Flash Flood (385 events) | CasCast | 0.072 | 25.619 | 0.961 | 0.0545 | 0.4660 |
| | Ours | 0.012 -0.060 | 38.378 +12.759 | 0.971 +0.010 | 0.0307 -0.0238 | 0.5140 +0.048 |

served. Both produce nearly zero-centered error distributions with similar likelihoods of over- and underestimation. The figure reflects a slight tendency to underestimate high-precipitation regions, consistent with average weather conditions; however, it overall indicates that ensemble members are well-spread around the ground truth.

Ensemble Performance Fig. S3 shows the per ensemble member MAE as well as the corresponding ensemble CRPS and MAE of the mean over ensemble members for the qualitative sample of Fig. 4 in the main paper. Across all lead times, the ensemble consistently outperforms the average performance of its individual members. This indicates that individual errors tend to spread around a common mean, and discrepancies cancel out when aggregated, yielding a mean forecast that closely aligns with the ground truth. This behavior is consistent with the error distributions discussed earlier.

Pixel Value Distributions Fig. S1 shows the distribution of LSM ensemble forecasts for pixels in low, medium, and

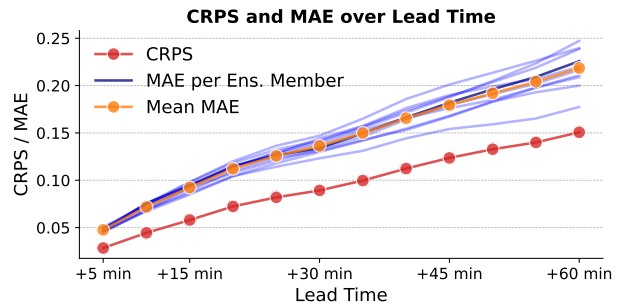


Figure S3. Forecast skill of the individual ensemble members and of their aggregated prediction for the example in Fig. 4. Each member constitutes a plausible realisation of the future weather, yet the expectation over ensemble members attains lower error.

high precipitation regimes. The mode shifts with the true intensity, and the variance increases for heavier rainfall, reflecting higher uncertainty in chaotic, high-precipitation re-

gions. All regimes exhibit a long tail toward larger values, capturing the possibility of intensifying rain; this tail becomes more pronounced for high precipitation. In this regime, however, the ensemble mean tends to underestimate the true value, consistent with climatology, where a decrease in intensity is more common than further escalation. Overall, the ensemble behavior aligns with known precipitation dynamics, indicating that our model has learned realistic weather statistics.

A.3. Performance on MeteoNet

In addition to the results obtained for the SEVIR [139] benchmark, we validate our model’s applicability to other datasets by applying our model to the MeteoNet [70] benchmark. Tab. 9 shows that our model performs similarly on MeteoNet and SEVIR. Further, our model outperforms all baselines but CasCast in terms of CRPS and achieves comparable CSI. However, we find that results on MeteoNet are highly sensitive to the chosen train–test split. Fig. S5 shows statistical differences between MeteoNet training splits. While differences are small, the date-based split shows a slightly higher mean, resulting in lower CSI for the random split as true negatives have no effect on CSI computation. Since CasCast [40] provides limited details on their experimental setup and no public MeteoNet checkpoint, we cannot fully validate comparability under their protocol. For this reason, we focus our main analysis on SEVIR.

Table 9. **Performance on MeteoNet:** Our approach achieves competitive performance on MeteoNet and performs similarly to the model trained on the SEVIR dataset. Yet, we observe a strong influence of the train-test split on downstream performance.

| Method | Split | CRPS↓ | SSIM↑ | HSS↑ | CSI↑ |
|--------------------------------|------------|--------|--------|--------|--------|
| EarthFormer [35] (NeurIPS ’22) | unknown | 0.0224 | – | – | 0.2831 |
| NowcastNet [158] (Nature ’23) | unknown | 0.0277 | – | – | 0.2955 |
| PreDiff [37] (NeurIPS ’23) | unknown | 0.0197 | – | – | 0.2546 |
| CasCast [40] (ICML ’24) | unknown | 0.0180 | – | – | 0.3156 |
| FREUD + LSM-L (ours) | Random | 0.0224 | 0.7212 | 0.0876 | 0.1117 |
| ↳ with cfg | | 0.0231 | 0.7133 | 0.1368 | 0.0876 |
| FREUD + LSM-L (ours) | Date-based | 0.0193 | 0.7312 | 0.2082 | 0.1417 |
| ↳ with cfg | | 0.0194 | 0.7405 | 0.3150 | 0.2191 |

A.4. Effect of Classifier-free Guidance

Impact on Performance We analyze the impact of classifier-free guidance (CFG) [48] on forecasting performance in Fig. S6, comparing our B-LSM to the state-of-the-art CasCast method [40]. As guidance strength increases, CRPS rises monotonically, reflecting reduced distributional coverage, consistent with observations in image generation [48, 93]. HSS, however, improves up to an optimal guidance level (1.5 for our model) before declining. We observe the same behavior with Adaptive Projected Guid-

ance (APG) [112], despite its design to counteract over-saturation in image synthesis at high guidance strengths.

Qualitative Effect We visualize two qualitative samples at different guidance scales with our method (Fig. S15 and Fig. S16) and CasCast (Fig. S17 and Fig. S18). For both methods, we observe that the extremeness of weather conditions increases with higher guidance. Samples degenerate into unrealistic extreme weather beyond a method-specific threshold. As APG does not solve this problem, we hypothesize that this behavior is distinct from over-saturation. Analyzing unconditional samples provided in Fig. S19, we find notably low precipitation intensity, as low precipitation is more common than strong rain. Hence, by applying guidance, we push samples from low to high precipitation.

Impact on Descriptive Statistics Inspired by these qualitative insights, we investigate the descriptive statistics of forecasts with different guidance scales in Fig. S7. For our method, we find that guidance consistently increases the average precipitation intensity in forecasts. For CasCast, we observe a different yet related behavior: while the mean intensity remains largely unaffected, extreme values increase dramatically, leading to unrealistically high precipitation that quickly exceeds the strongest precipitation found in the SEVIR dataset [139]. Therefore, both methods produce samples with unrealistically high precipitation with strong guidance, which is likely not an over-saturation artefact.

Unsuitability of CFG for Forecasting Based on our previous findings, we believe the problem with guidance in generative precipitation nowcasting is related to the dominance of low precipitation in the datasets. Generative models that learn the data distribution will tend to produce samples with low precipitation, resulting in unconditional samples with less intense precipitation than conditional samples. Therefore, when applying classifier-free guidance, we push samples towards higher precipitation, which leads to the observed unrealistic samples. Therefore, guidance is flawed in nowcasting, as the potential improved alignment with conditions is confounded by a distribution shift. Furthermore, guidance induces reduced distribution coverage and stronger overconfidence, which is problematic for uncertainty-aware forecasting of chaotic weather systems. This result is not limited to our method and applies to state-of-the-art approaches, such as CasCast [40], as well. Therefore, it is a general flaw of diffusion-based nowcasting. Notably, our method performs well without guidance, achieving superior distribution coverage and perceptual similarity at competitive localization compared to methods that rely on guidance (see Tab. 2 in main paper).

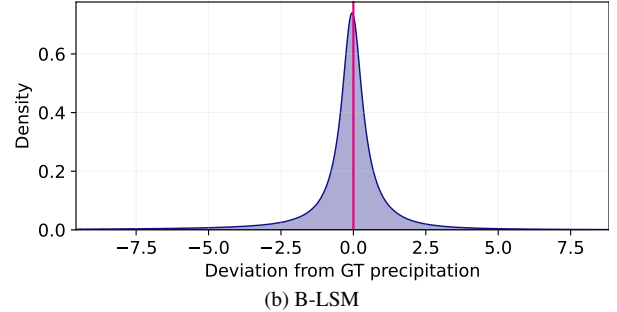
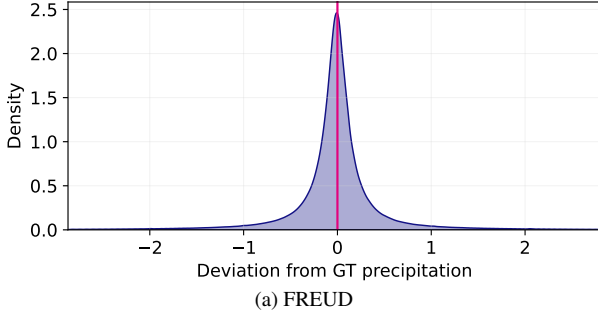


Figure S4. Deviations from ground truth precipitation, whereby 0 denotes a perfect forecast. Only pixels with more than 1 kg/m^2 precipitation are considered. The x-axis range indicates three standard deviations from the mean to remove outliers. Both distributions are almost zero-centered and show similar likelihoods of over- and underestimating precipitation.

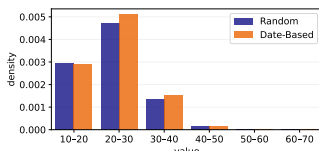


Figure S5. Training data distribution of MeteoNet splits.

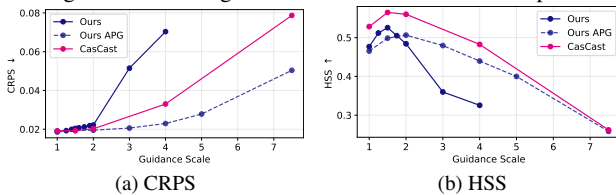


Figure S6. Performance of our B-LSM and CasCast with increasing CFG [48] and APG [112] guidance strength. For all approaches, CRPS continuously worsens while HSS improves up to an optimal value and deteriorates afterwards.

A.5. Further Ablations

Latent Space Distributions Fig. S8 shows the density distribution of the latent space for all regularization variants. Without regularization, we observe high norms and variance, resulting in low density and long tails. Moreover, we observe a bimodal distribution for all latent channels. The same bimodal pattern is observed with *KL-reg*. FREUD, but the variance is substantially reduced, leading to a higher density throughout the value range, and the distribution is almost zero-centered. However, we still observe long tails in the distributions. Similarly, the CasCast latent value distribution exhibits reduced variance and an almost zero-centered latent space; however, we still observe very long tails due to the weak KL regularization. In comparison, the *T-reg*. latent space exhibits the most zero-centered distribution with the lowest variance. We do not observe heavy tails and a less pronounced bimodal pattern; thus, the density remains high across the $[-1, 1]$ value range. This indicates that the *T-reg*. FREUD encoder produces a latent distribution that is easier to learn and sample for both the generative

Table 10. Comparison of forecasting skill with our B-LSM using factorized spatio-temporal attention and full self-attention. We find slightly improved performance with the full attention variant.

| Attention | CRPS↓ | SSIM↑ | HSS↑ | CSI↑ |
|------------|--------|--------|--------|--------|
| Factorized | 0.0196 | 0.7828 | 0.4923 | 0.3805 |
| Full | 0.0187 | 0.7897 | 0.4968 | 0.3848 |

decoder and downstream latent space model (see Tab. 5 in main paper).

Number of Conditioning Frames The masking-based training paradigm (RaMViD) [54] allows variable conditioning frames during inference. We find improved performance when using more conditioning frames in Fig. S9.

Full vs Factorized Attention We further train a latent space model with full attention over space and time, and compare it to our spatio-temporally factorized attention model in Tab. 10. Full attention provides slightly better performance, but its computational cost is prohibitive: The complexity of full self-attention is given by $(T \times H \times W)^2$, whereas the complexity of factorized attention is given as $(H \times W)^2 + T^2$. For our use case, we have $T = 25$, $H = 24$, and $W = 24$ after latent embedding and patching (see Sec. B), therefore, we require 207.4 GFLOPs for full attention and 0.3 GFLOPs for factorized attention. We believe that for operational nowcasting, such marginal improvements do not justify the substantial computational overhead; therefore, we only report results from the factorized model throughout the paper.

Blob Toy Experiment We emulate an experiment from prior work [14] to evaluate uncertainty quantification by inserting areas of unmoving extreme precipitation (blobs) into the data and assessing the variance of reconstruction ensembles. Fig. S10 shows a linear regression of the number of blobs against the ensemble variance. We find a significant linear correlation between ensemble variance and the blob count, confirming that reconstruction variance can de-

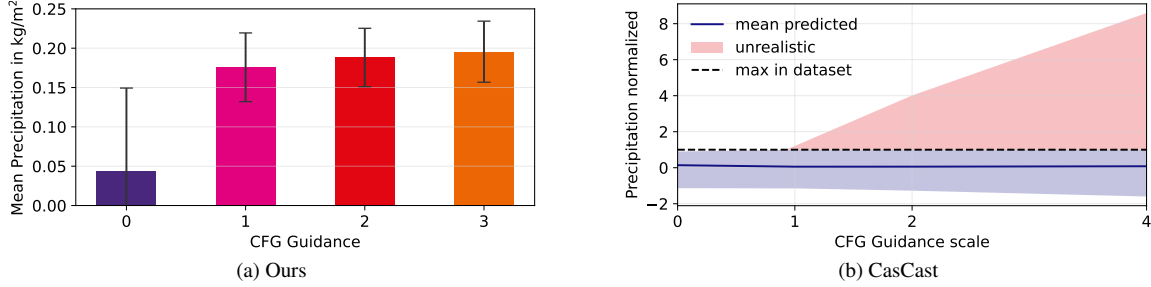


Figure S7. The effect of cfg [48] on our method and CasCast [40]. For our approach (a), the mean precipitation consistently increases while the ensemble variance (error bars) decreases. For CasCast (b), the mean remains largely unaffected, but the min-max range of predicted values (shaded area) explodes. We keep the encoded $[0, 1]$ range in the right plot instead of applying the non-linear mapping to precipitation for visualization.

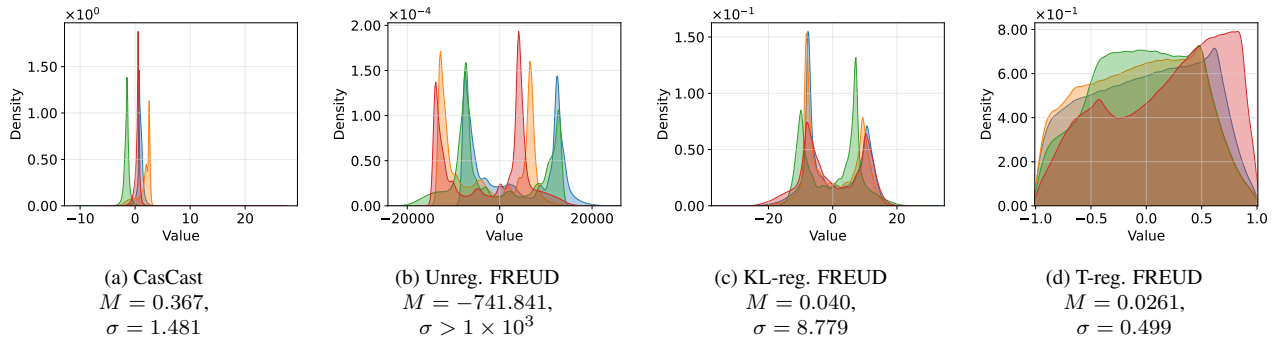


Figure S8. Latent space distributions for different regularization schemes and the CasCast encoder [40]. Colors indicate the latent space channel. The x-axis range denotes the min-max range of latent values.

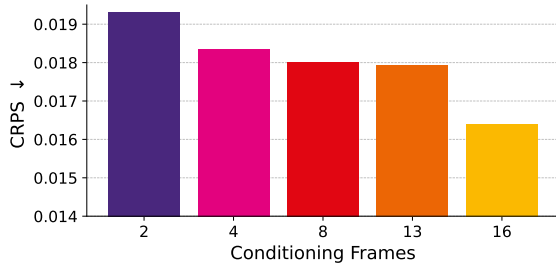


Figure S9. Performance of our forecasting pipeline for different numbers of conditioning frames.

test deviations from the training distribution.

We show qualitative samples of a reconstruction ensemble with blobs together with corresponding variance maps in Fig. S13 and Fig. S14. The variance maps display an outline of high variance surrounding blobs and lower variance within them. Therefore, variance is high where abnormal blobs interact with normal precipitation, as it is unclear how the precipitation will alter the blob shape. However, in the blob center, pixels are surrounded by extreme precipitation, leading to confidence in their extreme values. Due to the sharp outline, we can isolate abnormal patterns using vari-

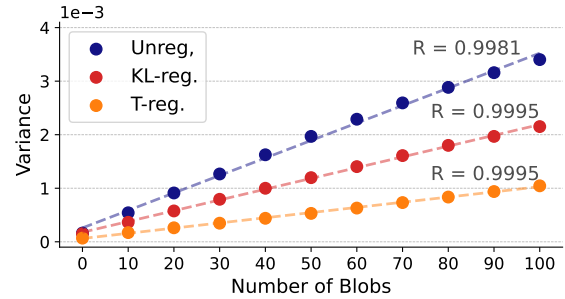
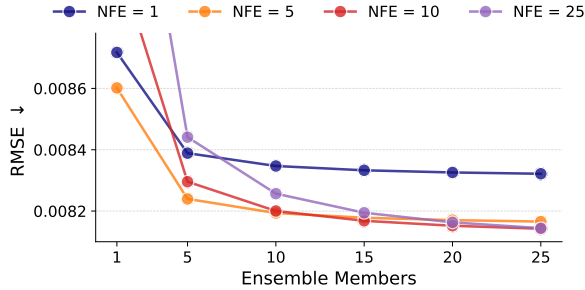


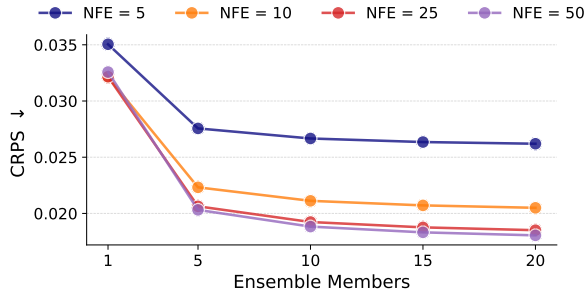
Figure S10. Intra-ensemble variance of first-stage reconstructions in the presence of increasing abnormal features (blobs). All linear regressions show significant correlations.

ance maps. Therefore, the FREUD reconstruction ensembles can successfully detect and localize abnormal patches.

Scaling Test-time Compute Fig. S11a shows the influence of the ensemble size and the number of sampling steps for each ensemble member on the reconstruction performance of FREUD. We observe a clear benefit from larger ensemble sizes, which plateau after 10 ensemble members. The sampling steps do not show a consistent effect, and



(a) FREUD



(b) B-LSM

Figure S11. Ablation of scaling test time compute by increasing the number of function evaluations (NFE) and the ensemble size for the compression stage and B-LSM. Larger ensembles consistently improve the performance, and more function evaluations improve performance for the LSM.

many-step runs are outperformed by few-step sampling for small ensemble sizes. Due to the strong conditioning from the encoder, the generative decoding task is simple, and the increased generative capabilities of expensive sampling runs are outweighed by integration errors, explaining the observed effect. Therefore, we can use efficient few-step sampling, which limits the overhead from using a generative decoder. However, ensemble size and function evaluations seem to be entangled, as runs with many function evaluations benefit more from larger ensembles. We find a good trade-off with five function evaluations, which performs best up to 20 ensemble members.

Similarly, we evaluate the effect of ensemble size and sampling steps on the latent space model in Fig. S11b. CRPS consistently improves with a larger ensemble size and more function evaluations. Yet, the benefit of using more than 25 sampling steps and 15 ensemble members is marginal, revealing diminishing returns. Still, these results highlight that we can improve forecasting performance by scaling test time compute, enabling flexibility in deployment depending on the requirements for accuracy and latency.

Ensembling inference cost Our method outperforms CasCast with a single decoder ensemble (cf. Tab. 2), yet

Table 11. Inference time per decoder ensemble size on a single H200 GPU.

| Ensemble size | 1 | 5 | 10 | 15 | 20 | 25 |
|-----------------------|-------|-------|-------|-------|-------|--------|
| Inference time (H200) | 0.63s | 2.49s | 4.83s | 7.18s | 9.56s | 11.93s |

Table 12. Comparison of RaMViD to Diffusion Forcing training. RaMViD training yields better downstream forecasting skill across all metrics.

| Training Paradigm | CRPS | SSIM | HSS | CSI |
|-------------------|--------|--------|--------|--------|
| Diffusion Forcing | 0.0218 | 0.7759 | 0.4627 | 0.3544 |
| RaMViD | 0.0196 | 0.7828 | 0.4923 | 0.3805 |

Fig. S11a shows larger ensembles improve performance. Since decoding is highly parallelizable, ensembling incurs limited wallclock overhead. Tab. 11 shows the evolution of wallclock latency with ensemble size. Even producing 25 decoder ensemble members requires less than 12 s inference time, remaining compatible with operational 5 min nowcasting.

Comparison with Diffusion Forcing Our masking-based training paradigm (RaMViD [54], see Sec. 3.3) can be interpreted as a special case of *Diffusion Forcing* [15]. In Diffusion Forcing, each frame is assigned an independent diffusion timestep during training. This offers more flexibility at inference time, as frames can be denoised using standard full-sequence, autoregressive, or rolling denoising. RaMViD can be interpreted as a variant of Diffusion Forcing, where during training, each frame is assigned either timestep $i = 1$ or timestep $i = \tau$, and during inference, each frame is initialized with a diffusion timestep $i = 1$ (data without noise) or $i = 0$ (pure noise).

We implement a variant of our model trained using Diffusion Forcing. Since our use case is forecasting, we further bias the sampling of per-frame timesteps so that temporally later frames tend to be assigned lower timesteps. Thus, on average, early frames are less noisy than later frames. This resembles the forecasting task at inference time. Tab. 12 compares RaMViD inference with the more flexible Diffusion Forcing approach using a B-LSM. We find superior performance with our masking-based training compared to the Diffusion Forcing setup across all metrics.

Table 13. Small (S), Base (B), and Large (L) latent space model (LSM) configurations.

| Model | Layers | Hidden size | Attention Heads | Parameters |
|-------|--------|-------------|-----------------|------------|
| S-LSM | 12 | 384 | 6 | 44M |
| B-LSM | 12 | 768 | 12 | 141M |
| L-LSM | 24 | 1024 | 16 | 473M |

B. Implementation Details

In the following, we provide additional implementation details and hyperparameter settings.

B.1. Architecture

FREUD The FREUD encoder uses a 4×4 spatial patching followed by a downsampling layer, which is implemented as two transformer blocks with a hidden dimension of 96 and three attention heads, followed by a PixelShuffle [119] operation to halve the resolution. Thus, we achieve a total of $8 \times$ downsampling along both spatial dimensions. The downsampling layers use neighborhood attention, where each pixel can only attend to a 7×7 spatial neighborhood. 2D Axial RoPE is used for positional embeddings. The encoder processes the downsampled inputs with four additional transformer blocks [28] with 384-dimensional tokens, six attention heads, and full self-attention to produce the final latent embeddings. For *T-reg*. FREUD, we additionally apply a Tanh function to the result and add a noise perturbation with $\sigma = 0.001$ to the latents. This small value is chosen to minimize adverse effects from perturbation and was not tuned or further ablated.

The FREUD decoder architecture is inspired by the Hourglass Diffusion Transformers (H-DiT) [24], which enable efficient diffusion in pixel space with a transformer architecture. The FREUD decoder employs downsampling, similar to the encoder, with a $1 \times 4 \times 4$ patching and a downsampling layer. The decoder downsampling layer uses spatio-temporally factorized [10] neighborhood attention [45] with a 7×7 spatial and a 3-step temporal neighborhood. Therefore, each frame only attends to the immediate neighbor frames. In the bottleneck, we use 12 DiT blocks after concatenating the encoder latents channel-wise to the decoder feature maps. The upsampling layers of the decoder are built in parallel to the downsampling layers and use Token Split [119] operations for upsampling.

Latent Space Model The LSMs operate in the latent space of the FREUD first-stage. For improved convergence speed, we normalize latents to zero mean and unit variance with offsets determined on the training dataset. The LSMs use a standard DiT architecture [84, 99] with 2×2 patching. The specific settings for all model sizes are provided in Tab. 13. We use 3D Axial RoPE and factorized spatio-temporal attention for all variants.

B.2. Training

Multi-stage Training Training transformers on high-resolution spatio-temporal nowcasting data is expensive [35]. Exploiting RoPE’s sequence length generalization capabilities [47, 132] and following current video training paradigms [135], we adopt a curriculum of training on progressively longer clips. We first pre-train FREUD and LSMs on single frames, and then progressively increase the number of frames per clip, until we finally train on the full sequence. During LSM image pre-training, we employ a standard unconditional diffusion training, which strengthens the model’s spatial understanding before introducing the need to understand temporal dependencies. FREUD gains only slightly from full-sequence training, showing good length generalization, whereas the LSMs improve substantially when training on the full sequence. We train the FREUD encoder for 250k iterations and the LSM for 350k iterations.

Additional Hyperparameters We train with the AdamW [82] optimizer setting $\beta_1 = 0.9$ and $\beta_2 = 0.99$. We use bfloat16 precision in training for efficiency. Image pretraining uses a 160 batch size on a single 40 GB A100. Later stages are run with a global batch size of 128. We use the Warmup-Stable-Decay (WSD) learning rate scheduler [55].

Outlier punishment Similar to MovieGen [135], we initially find spot artifacts in reconstructions in our FREUD first stage. Therefore, we adopt the outlier punishment from MovieGen and penalize deviations of latent values from the latent mean if they exceed r standard deviations. Following [135] we use

$$\mathcal{L}_{OPL}(\theta) = \frac{\sum_{i=1}^{H_l} \sum_{j=1}^{W_l} \max \left[\left| \|\mathbf{z}_{i,j} - \text{mean}(\mathbf{z})\| - r \|\text{Std}(\mathbf{z})\|, 0 \right]}{H_l \cdot W_l}$$

where H_l and W_l are the dimensions of the latent embeddings, and $\mathbf{z} \in \mathbb{R}^{C_l \times H_l \times W_l}$ are the frame-wise latents. In practice, we set $\lambda_{OPL} = 10^5$ to a large value and use $r = 3$ as a common value in outlier detection. We observe \mathcal{L}_{OPL} contributes only in the beginning of the training.

B.3. SEVIR dataset

The SEVIR dataset [139] is a weather observation dataset particularly well-suited for evaluating precipitation nowcasting methods because approximately 20% of the 20,393 weather events are taken from NOAA’s Storm Event Database [94] and, hence, represent extreme weather. For the remaining 80% of the dataset, random events are sampled while giving a higher probability to high precipitation events. All events are drawn from the 2017–2019 time range and are recorded over the Continental United States.

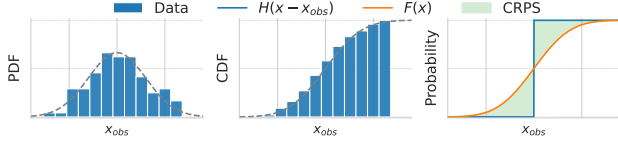


Figure S12. Schematic illustration of CRPS.

Each event covers a 384×384 km region over a 4 h timespan. To indicate precipitation, SEVIR uses the NEXRAD radar mosaic of Vertically Integrated Liquid (VIL). VIL is recorded with 1 km spatial and 5 min temporal resolution.

We use the same test data as Earthformer and CasCast [35, 40] to calculate our metrics and use the remaining data for training. Following previous work [35, 40, 115], we use 13 frames (65 min) as the conditioning to predict the next 12 frames (60 min) of precipitation unless specified otherwise. For the training data, we differ from previous work in taking exhaustive subsequences from each event. As recommended by the dataset creators [139], we keep the non-linear encoding of VIL from SEVIR and normalize the encoded $[0, 255]$ values to the $[-1, 1]$ range. At inference time, we can revert the normalization and apply the non-linear mapping

$$x_{kg/m^2} = \begin{cases} 0, & \text{if } x_{pixel} \leq 5 \\ (x_{pixel} - 2)/90.66, & \text{if } 5 < x_{pixel} \leq 18 \\ \exp((x_{pixel} - 83.9)/38.9) & 18 < x_{pixel} \end{cases}$$

to obtain the VIL in kg/m^2 [139].

For consistency with previous work [35, 40, 115] and alignment with the SEVIR data [139], we use $H = W = 384$, $C = 1$, $L^{in} = 13$, $L^{out} = 12$, and $T = 25$ unless specified otherwise.

B.4. Metrics details

To ensure comparability, we use the evaluation pipeline implemented by Gong et al. for the CasCast paper [40].

CRPS We calculate the CRPS to measure the alignment of the predicted distribution with the ground truth distribution. CRPS is a generalization of the Mean Absolute Error (MAE) to probabilistic predictions. CRPS is calculated as

$$\begin{aligned} CRPS(F, x) &= \int_{-\infty}^{\infty} (F(y) - \mathbf{1}_{y \geq x})^2 dy \\ &= \mathbb{E}_{X \sim F} [||X - x||] - \frac{1}{2} \mathbb{E}_{X, X' \sim F} [X - X'] \\ &\approx \frac{1}{N} \sum_{i=1}^N |f_i - x| - \frac{1}{2N^2} \sum_{i=1}^N \sum_{j=1}^N |f_i - f_j|, \end{aligned}$$

where x is the observed value, $F(y)$ is the cumulative distribution function of the forecast, and $\{f_1, \dots, f_N\}$ is the ensemble of forecasts. We show a schematic illustration of

CRPS in Fig. S12. Essentially, CRPS is the squared error between the ground truth cumulative distribution and the predicted cumulative distribution, which can be approximated with a finite ensemble using the MAE of the forecast and subtracting the MAE of ensemble members.

SSIM Further, we use the Structural Similarity Index Measure (SSIM) to measure visual similarity between the ground truth precipitation and the forecast. SSIM for data with a single channel is calculated as

$$SSIM(x, y) = \frac{(2\mu_x\mu_y + C_1)(2\sigma_{xy} + C_2)}{(\mu_x^2 + \mu_y^2 + C_1)(\sigma_x^2 + \sigma_y^2 + C_2)},$$

where x is the ground truth and y is the prediction, μ_x and μ_y are the average intensities, σ_x^2 and σ_y^2 are the variances of intensities, σ_{xy} is the covariance between the images and C_1 and C_2 are two small constants for numerical stability. SSIM is calculated by averaging results from a sliding window across the image and using Gaussian weighting to calculate means and variances, whereby the largest weight is assigned to the central pixel.

HSS and CSI We use the Heidke Skill Score (HSS) and Critical Success Index (CSI) computed on a per-pixel basis to identify positional inaccuracies. HSS is calculated as

$$HSS = \frac{2(TP \cdot TN - FP \cdot FN)}{(TP + FN)(FN + TN) + (TP + FP)(FP + TN)}.$$

Here, the True Positives (TP), False Positives (FP), False Negatives (FN), and True Negatives (TN) are calculated with respect to some threshold. To obtain the reported HSS, we average HSS values calculated using six thresholds (16, 74, 133, 160, 181, 219). HSS indicates improvement of a prediction over random chance, where 0 indicates no forecasting skill beyond chance and 1 indicates a perfect forecast.

CSI or Threat Score quantifies the proportion of correctly predicted events while excluding true negatives, which makes it useful in scenarios where non-events (e.g., no precipitation) are more common than true events. CSI is calculated as

$$CSI = \frac{TP}{TP + FP + FN}.$$

Again, we report the CSI averaged over the six thresholds.

C. Limitations

Our method achieves superior distribution coverage and perceptual similarity as measured by CRPS and SSIM. However, especially the smaller models underperform for localization-centric metrics such as HSS and CSI, which aligns with previous work suggesting a trade-off between

localization and distribution coverage [153]. While our method achieves a superior trade-off compared to prior work, future work could explore introducing different conditionings and priors that improve localization while keeping full distribution coverage. A possible solution might be to use noisy prior frames as the starting point for flow matching [76], which, however, is non-trivial with non-autoregressive video modeling, as in RaMViD.

Our method yields more accurate and better-calibrated forecasts than the current state-of-the-art. Furthermore, FREUD can quantify reconstruction uncertainty at inference time, which was not possible with previous VAE-based compression stages. Sampling from the FREUD decoder achieves better calibration than samples from a VAE. Still, our forecasts and FREUD reconstructions exhibit some overconfidence. Therefore, future work should focus on developing calibration methods for generative flow models. Related to this problem, our method, as well as prior methods, tend to underestimate precipitation. As generative models learn the distribution of the training data, this is expected because low precipitation is more common than extreme precipitation. Therefore, future work should explore options to better align the forecast distribution with the ground truth in rare extreme scenarios.

Previous work has solved this problem using *cfg* [48]; however, we find that the use of *cfg* is flawed in precipitation nowcasting, as increasing *cfg* leads to higher precipitation independent of the conditioning. This holds for our method as well as our strongest competitor, CasCast (see Sec. A.4). Therefore, the use of *cfg* does not yield improved alignment with conditions, but rather increases intensity. Follow-up research should identify better guidance mechanisms that enable the generation of realistic forecasts that align with actual conditions.

As with all generative models, our approach inherits the statistical properties of its training data. Since high-quality weather datasets are primarily collected in technologically advanced regions with dense radar coverage, nowcasting methods for precipitation that rely on radar observations - including ours - are inherently limited to areas with such infrastructure, leaving large parts of the world (e.g., oceans and many developing regions) underserved. Future work should explore conditioning strategies that do not depend solely on radar. Cloud-top temperatures from geostationary satellites offer near-global coverage [134], and decades of research have demonstrated their utility for estimating precipitation in radar-sparse regions [52, 60, 87, 113]. These alternative conditioning signals present a promising path toward globally applicable precipitation nowcasting.

D. Weather Forecasting Literature Review

Weather nowcasting refers to short-term weather forecasting for periods of 30 min to 12 h, with high temporal and spatial resolution [31, 37, 40, 71]. Traditionally, numerical weather prediction (NWP) systems, which simulate atmospheric evolution by numerically solving physical equations, have set the state-of-the-art for this task [29, 31, 108, 125]. NWPs approximate solutions by averaging over spatial regions. For low-latency forecasts, higher down-sampling is required, resulting in reduced resolution [74]. Further, the inherent non-linearity in atmospheric dynamics [69, 91, 131] implies that minor perturbations or sensor inaccuracies will lead to exponential divergence over time [64, 81, 96]. Therefore, NWPs are run multiple times with slightly altered inputs to estimate uncertainty, exploding computational costs. As a computationally efficient alternative to NWPs, extrapolation-based techniques using optical flow are used [22, 39, 114, 146, 147]. While these methods are much faster to compute, they are flawed because optical flow cannot model the formation and dissipation of weather patterns, limiting their predictive capability.

To overcome the limitations of traditional methods, recent work has turned to deep learning for efficient precipitation nowcasting. These approaches typically fall into two categories: *deterministic* and *probabilistic* models. Deterministic nowcasting refers to models that make a single prediction based on the input and do not account for uncertainty in their predictions. In contrast, probabilistic nowcasting methods usually employ generative models to produce samples of possible outcomes, which allows for estimating uncertainty through repeated sampling.

D.1. Deterministic

Recurrent In an early work, Shi et al. [120] propose the ConvLSTM architecture, which extends the traditional LSTM [51] with convolutions to retain spatial structure. With this modification, they outperform a traditional optical flow-based nowcasting system [146]. Later, they proposed the TrajGRU [121], which improves the previous method by replacing fixed-size convolution with learned warping. The PredRNN [144] extends ConvLSTMs with a dual memory mechanism, integrating short-term cell and long-term memory, to better capture complex spatio-temporal dependencies. PhyDNet [42] outperforms the previous methods by learning a latent space with known dynamics, evolving the latent state according to these laws, and using a ConvLSTM to correct inaccuracies.

Convolutional Differing from the previous methods, Agrawal et al. [1] formulate nowcasting as an image-to-image translation problem and use a convolutional Unet architecture [111] with timesteps concatenated along the channel dimension. Their method outperforms optical flow

and a low-latency NWP [29]. Trebing et al. [136] improve computational efficiency by factorizing spatio-temporal attention and convolutions, reducing the number of parameters while retaining competitive performance. In contrast, Fernández & Mehrkanon [33] explicitly model the temporal dimension using 3D convolutions instead of channel-wise concatenation and retain computational efficiency by factorizing 3D convolution into three axial convolutions. Additionally, convolutions with increasing dilation are used in the bottleneck. Their method outperforms the previous convolutional approaches, highlighting the advantage of temporal modeling. Gao et al. propose "simpler yet better video prediction" (SimVP) [36], which uses a frame-wise encoder and decoder and a convolution-based bottleneck model that captures temporal evolution. Their approach outperforms recurrent models [42, 120, 144], underscoring the advantage of treating nowcasting as image translation.

Transformers Yang et al. [151] propose a TransUnet [17] architecture for nowcasting where transformer blocks [28, 138] are used in a Unet bottleneck. They further augment the Unet with attention and apply factorized convolutions, resulting in improved performance over a standard TransUnet and previous convolutional Unet architectures, revealing benefits of transformer-based modeling. Discarding convolution entirely, Gao et al. [35] introduce the Earthformer model with cuboid attention for efficient processing of high-resolution spatio-temporal data. Cuboid attention is applied to fixed-size spatio-temporal regions independently, and communication between cuboids is facilitated by global self-attention over class tokens. Their approach outperforms convolutional [1] and recurrent [42, 120, 144] architectures, cementing the advantage of attention-based modeling. Similarly, Pathak et al. [97] also adopt a ViT-based [28] architecture but compute self-attention in the Fourier domain for efficiency. They outperform a state-of-the-art NWP [109] for small-scale variables such as precipitation, demonstrating the superiority of deep learning for nowcasting.

Classification In contrast to the previous methods, Sonderby et al. [125] treat nowcasting as classification and predict a SoftMax probability distribution over discrete intensity bins. Their approach, MetNet, conditions on a large spatial context of previous precipitation, cloud-top temperatures, and topology and uses a spatial encoder for efficient processing with a bottleneck ConvLSTM and Axial Self-Attention [49]. MetNet-2 [31] uses an even larger context, and an additional sequence of convolutions with increasing dilation to outperform a state-of-the-art NWP ensemble [89] over the entire lead time range up to 12 h, demonstrating the flexibility of deep learning-based nowcasting.

The major drawback of these deterministic methods is their lack of accurate uncertainty quantification. Methods trained with regression losses minimize the mean difference

between predicted and observed values, where the minimizer is given as the expectation over the outcome, leading to mode averaging, which results in blurry predictions. Models trained with a classification objective mitigate this problem, but the pixel-wise objective does not exploit spatial dependencies and cross-correlations. In addition, Soft-Max probability distributions suffer from suboptimal calibration [57].

D.2. Probabilistic

GAN nowcasting As a solution, Ravuri et al. [107] propose to use a conditional Generative Adversarial Network (GAN) [41, 88] with a temporal and spatial discriminator for nowcasting, where samples from the model are sharp and multiple samples can be produced to quantify uncertainty. Compared to deterministic methods such as MetNet [125] and Unet [1], and extrapolation (exemplified by PySteps [59, 104]), their method, Deep Generative Models of Radar (DGMR), achieves superior accuracy, calibration, and expert evaluation. Ji et al. [61] propose a ConvLSTM-based GAN model that outperforms optical flow and ConvLSTM for heavy precipitation events, underscoring the importance of probabilistic modeling in critical extreme situations. Liu et al. [79] propose GAN-based forecasting with conditioning on a deterministic forecast, resulting in sharpened forecasts compared to the deterministic-only approach. A similar approach is proposed by Price & Rasp [102] who condition a GAN on a low-resolution NWP ensemble forecast to produce a high-resolution prediction. Their method is superior to simple interpolation and convolution-based upsampling and approaches the performance of a state-of-the-art NWP [89] with drastically reduced complexity. Finally, Zhang et al. [158] propose NowCastNet, which combines a differentiable extrapolation with a learned residual and a stochastic GAN refiner. Their approach outperforms previous deterministic [144], probabilistic [107], and extrapolation-based [59, 104] methods according to quantitative metrics and expert evaluations, highlighting the importance of sharp generative forecasts for downstream deployment.

While these works hint at the importance of probabilistic modeling for nowcasting, they rely on GANs, which are known to suffer from mode collapse [66]. Therefore, the samples from these models will underestimate the true weather variance. Further, they might neglect additional smaller modes in the true weather distribution, which are particularly important in nowcasting rare extreme weather events. Therefore, these models fail to capture the full distribution of future weather evolution.

Diffusion-based nowcasting To tackle this problem, Leinonen et al. [71] use a diffusion model with a solid mathematical foundation [50, 124] and empirically high sample variance [50, 93] for nowcasting. Due to the com-

plexity of iterative sampling, they opt for a latent diffusion approach [110], and apply diffusion in the latent space of a VAE compression model. Their generative model is conditioned on a deterministic prediction, which is augmented by the diffusion model. This architecture outperforms GAN-based nowcasting [107], especially for detecting extreme weather events. Similarly, Gao et al. [37] use a latent diffusion approach for their PreDiff architecture, but discard the deterministic conditioning in favor of physics-based guidance and conditioning on previous precipitation maps. Their approach consistently outperforms a range of deterministic [1, 35, 42, 120, 144] and GAN-based [107] approaches.

Since these early successes, architectural modifications have been proposed. Asperti et al. [7] suggest a learned aggregation of ensemble members instead of the canonical mean, while She et al. [115] integrate a transformer block from a large vision language model to ease training. Nai et al. [90] identify classifier-free guidance [48] as an option to improve forecasting skill. Moreover, Ling et al. [77] raise concerns about latent diffusion, as the cascaded architecture can lead to error accumulation and unquantified uncertainty. As an alternative, they suggest training the model end-to-end while integrating conditioning by concatenating feature maps from an condition encoder model.

Diffusion has also been used for longer-range forecasts. Li et al. [74] forecast precipitation over 16 days with a latent diffusion model conditioned on a deterministic forecast and outperform two NWP approaches [100, 162], cementing diffusion-based weather forecasting as a viable alternative to simulation. Further, Stock et al. [130] show that by auto-regressively unrolling a 1 h ahead diffusion-based forecast, reasonable forecasts up to 60 days lead time can be obtained and seasonal patterns are captured in year-long rollouts, indicating a robust understanding of the weather system in diffusion models. Similarly, Shi et al. [118] outperform a range of deterministic baselines [19, 92, 97, 140] with auto-regressive modeling conditioned on only two initial states. Building on this success, Price et al. [103] introduce GenCast as a follow-up to GraphCast [68], providing 15-day global forecasts of 25 variables with 27 km spatial and 12 h temporal resolution. The model is conditioned on two previous states, forecasts auto-regressively, and uses a Graph Transformer [156] backbone. They outperform a top-of-the-line ensemble NWP system [89], demonstrating the superiority of deep-learning-based generative forecasting with diffusion. Recently, Alet et al. [5] proposed *Functional Generative Networks* (FGN) as a follow-up to GenCast. They independently train an ensemble of predictors to account for epistemic uncertainty. To model aleatoric uncertainty, the authors turn the ensemble members themselves probabilistic by sampling a low-dimensional noise vector and injecting it via conditional normalization lay-

ers, effectively acting as a structured weight perturbation. The models are then trained directly using CRPS as the loss function, encouraging the models to make accurate and diverse predictions. The proposed model outperforms GenCast while providing substantially faster generation. Their results call the current dominance of diffusion-based approaches into question, although it remains unclear how well this approach transfers to domains where fine-scale stochasticity plays a larger role, such as precipitation nowcasting.

D.3. Cascaded deterministic-probabilistic

Early results show that conditioning a diffusion model on a deterministic forecast yields high-quality forecasts [18, 71, 72, 74, 77, 118]. Yu et al. [153] analyze these results and determine that probabilistic diffusion-only approaches show superior distribution coverage and sharpness than deterministic forecasts, but often suffer in terms of accurate localization. Building on physical knowledge, they suggest using a diffusion model to predict the residual between a deterministic forecast and the ground truth and find improved performance over deterministic-only [35, 36] or diffusion-only [37] approaches. Similarly, CasCast [40] conditions a latent space diffusion transformer [99] on a deterministic forecast and applies sequence-wise diffusion transformer blocks after spatial encoding. Their model consistently outperforms deterministic [35–37, 42, 120], GAN-based [157], and diffusion-only [37] nowcasting methods. Inspired by these results, Pathak et al. [98] condition an auto-regressive diffusion model on a deterministic initial forecast, and find their model outperforms a low-latency NWP [29]. However, they also indicate their method is overconfident and not well calibrated, hinting at a disadvantage of cascaded architectures.

We improve upon these prior works by compressing pixel-space data into a low-resolution latent space while quantifying the uncertainty from compression [77]. Further, we avoid biasing the generation with a deterministic forecast [98] and aim to achieve similar localization by exploiting the advantages of transformer-based architectures that allow to exploit conditioning more effectively with self-attention.

E. Uncurated Qualitative Results

In the following we provide further qualitative samples.

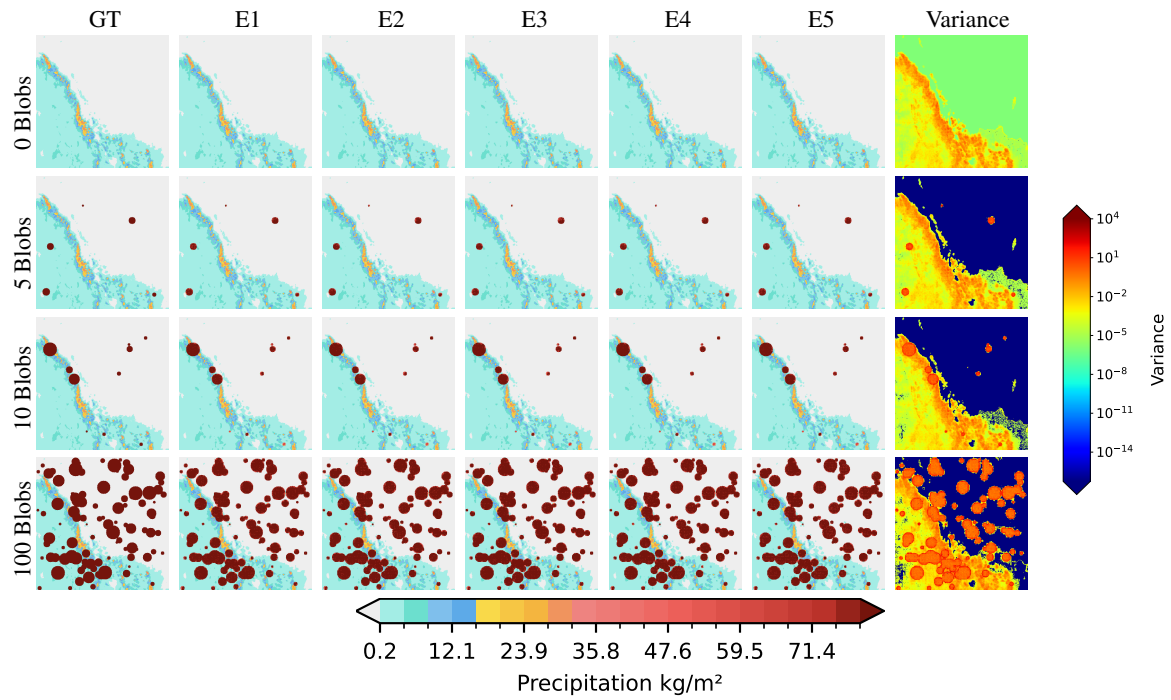


Figure S13. Qualitative results for blob experiment. The variance around blobs is high. Therefore, our first stage can localize abnormal features using ensemble variance. Best viewed zoomed in.

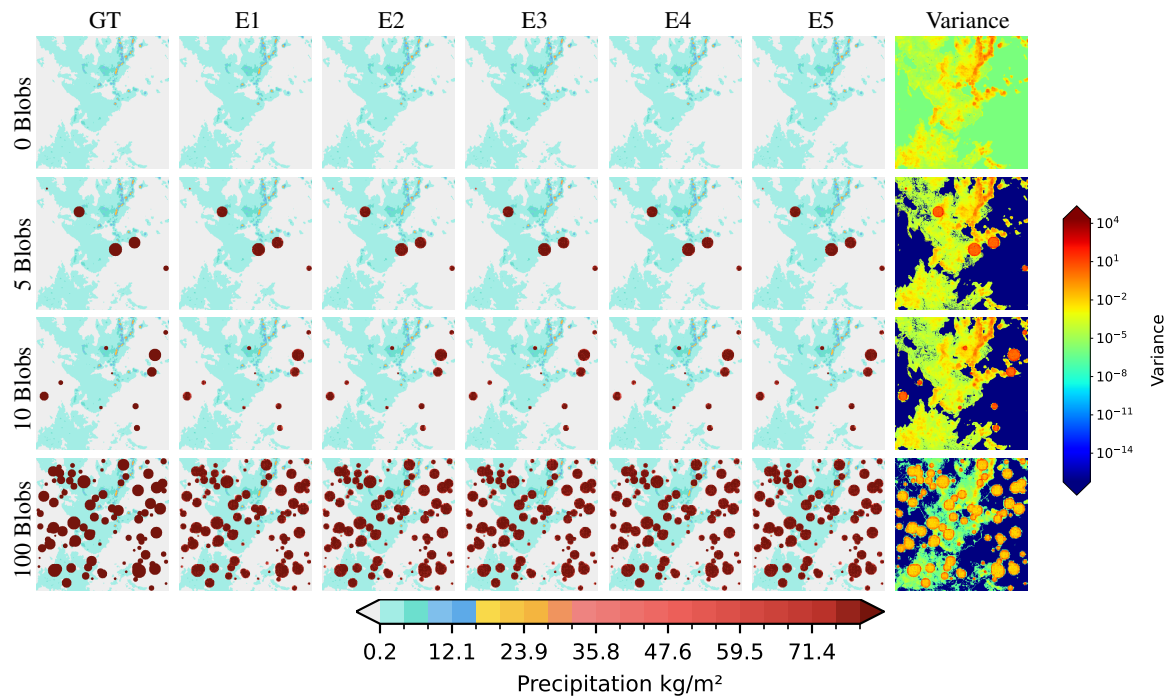


Figure S14. Qualitative results for blob experiment. The variance around blobs is high. Therefore, our first stage can localize abnormal features using ensemble variance. Best viewed zoomed in.

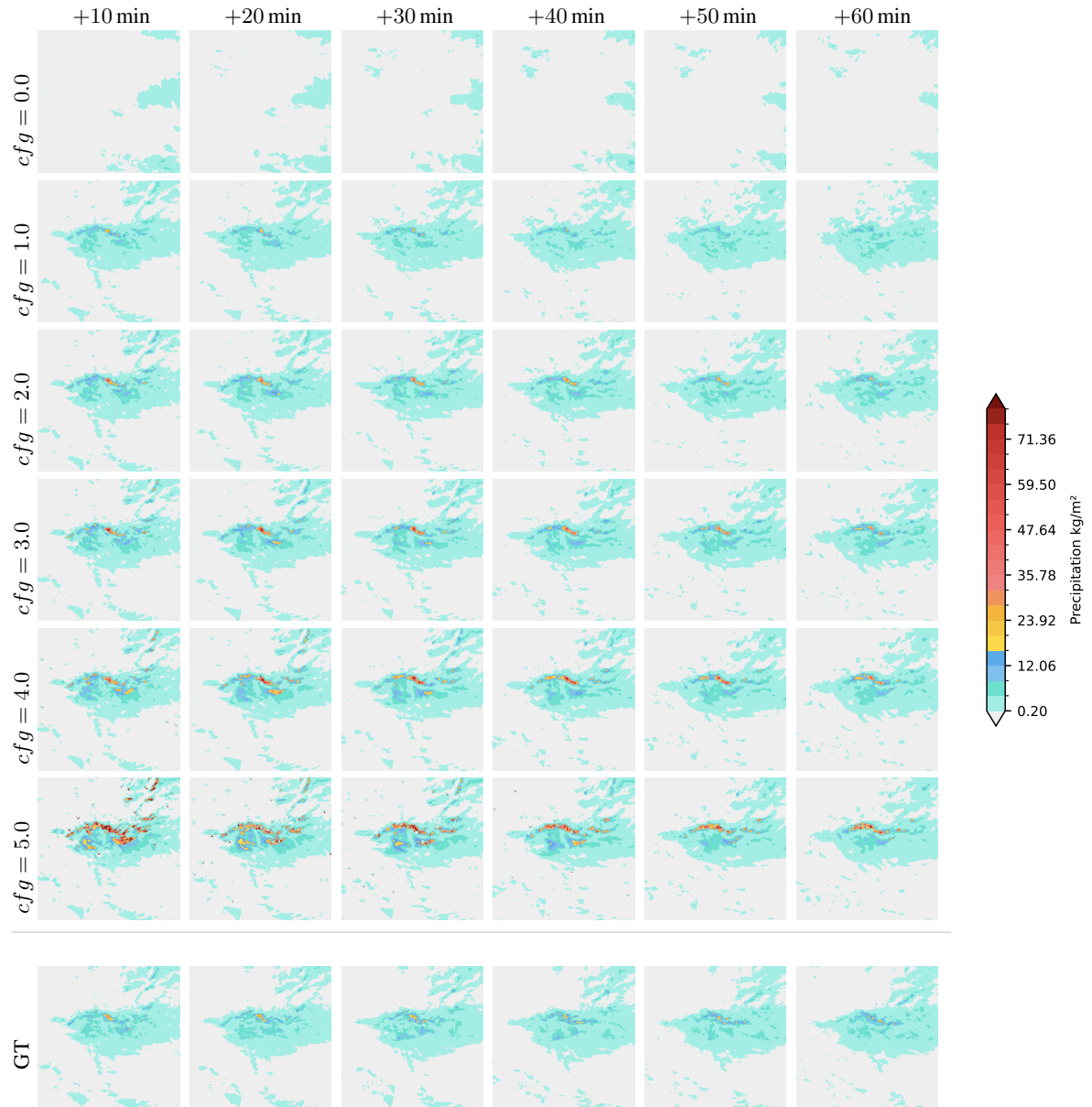


Figure S15. Qualitative results obtained with our B-LSM in the *T-reg.* latent space for different guidance scales [48]. Guidance 0.0 indicates unconditional sampling, while guidance 1.0 indicates conditional sampling without guidance. Best viewed zoomed in.

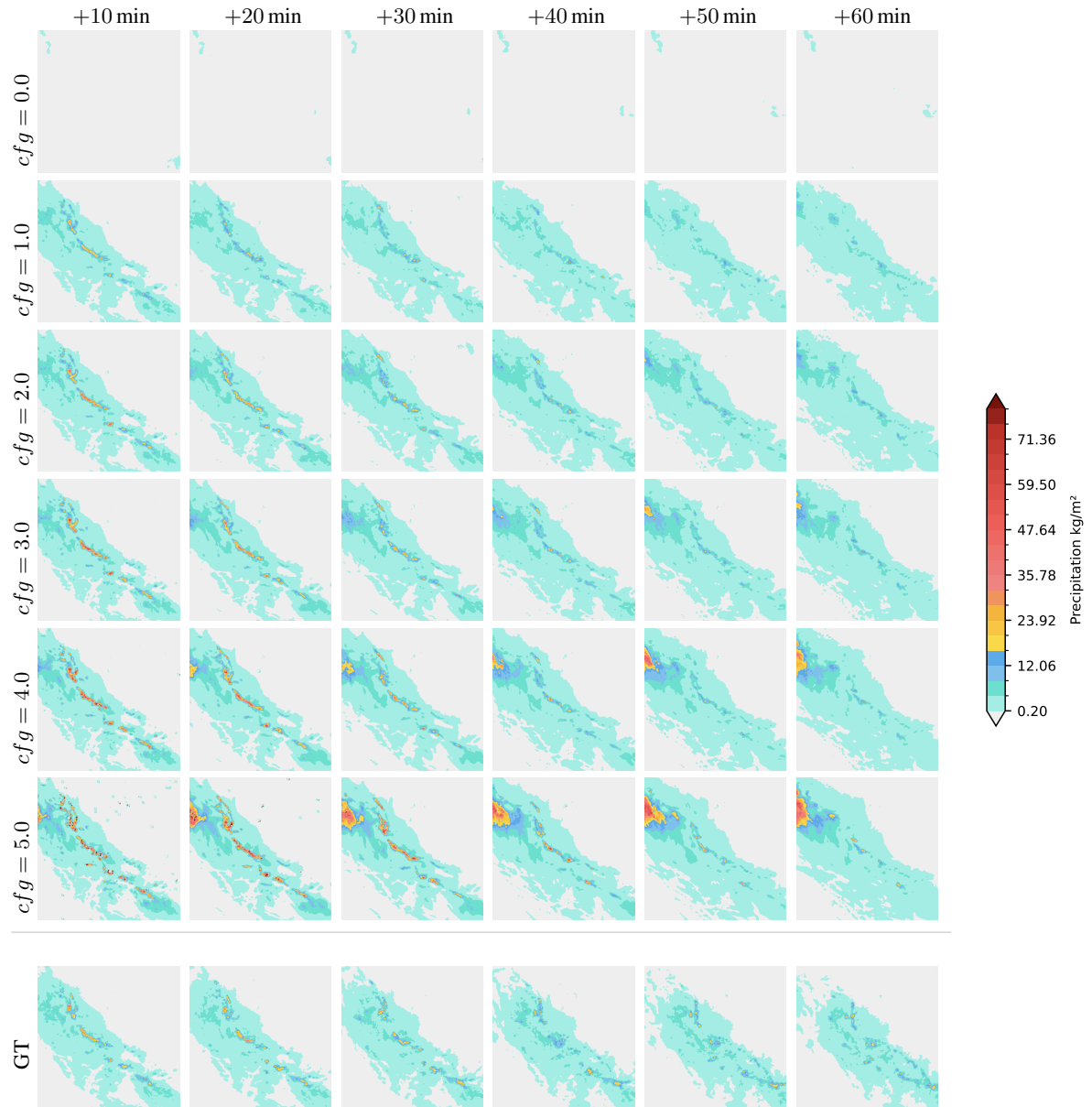


Figure S16. Qualitative results obtained with our B-LSM in the *T-reg.* latent space for different guidance scales [48]. Guidance 0.0 indicates unconditional sampling, while guidance 1.0 indicates conditional sampling without guidance. Best viewed zoomed in.

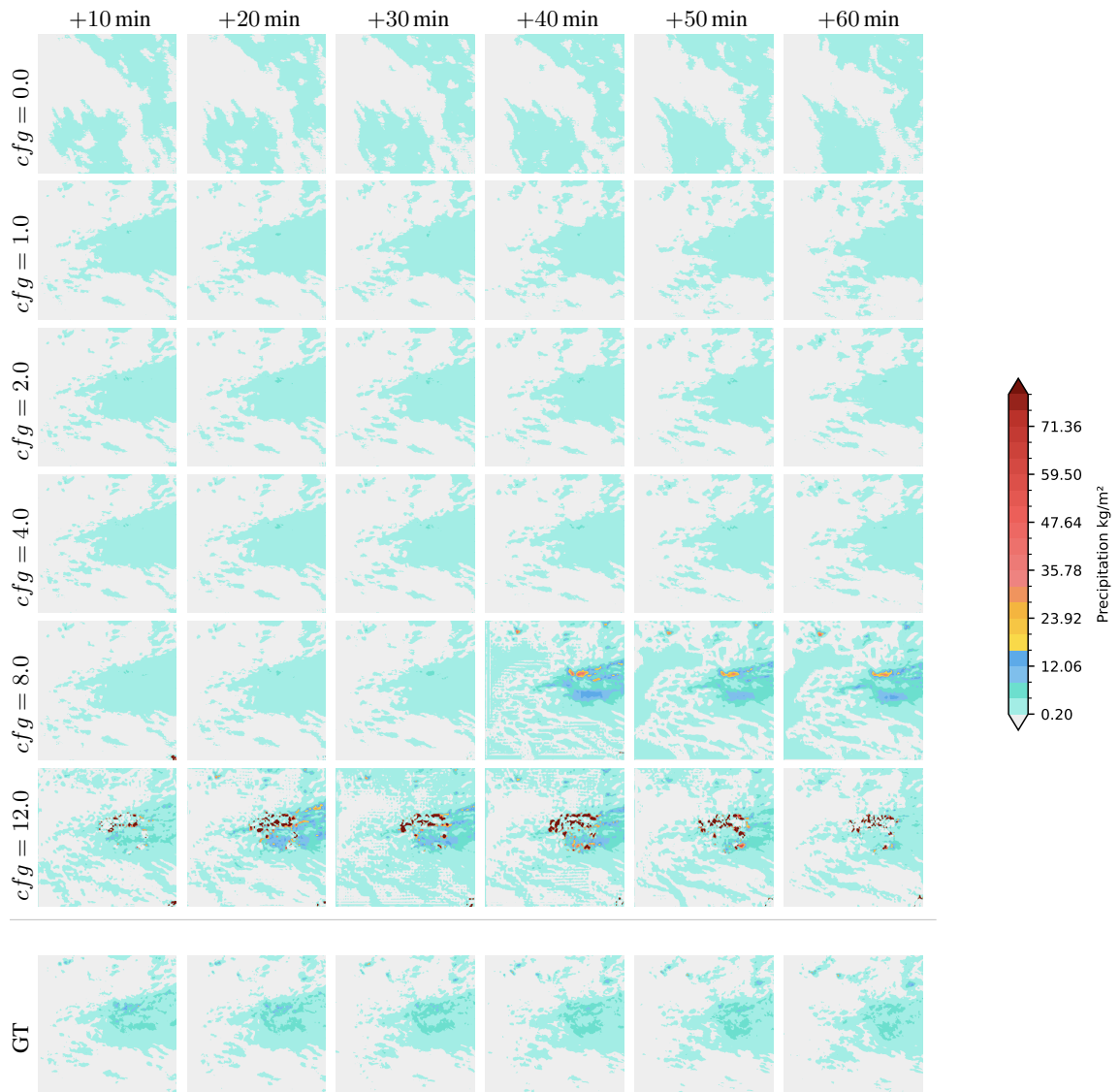


Figure S17. Qualitative results obtained with **CasCast** [40] for different guidance scales [48]. Guidance 0.0 indicates unconditional sampling, while guidance 1.0 indicates conditional sampling without guidance. Best viewed zoomed in.

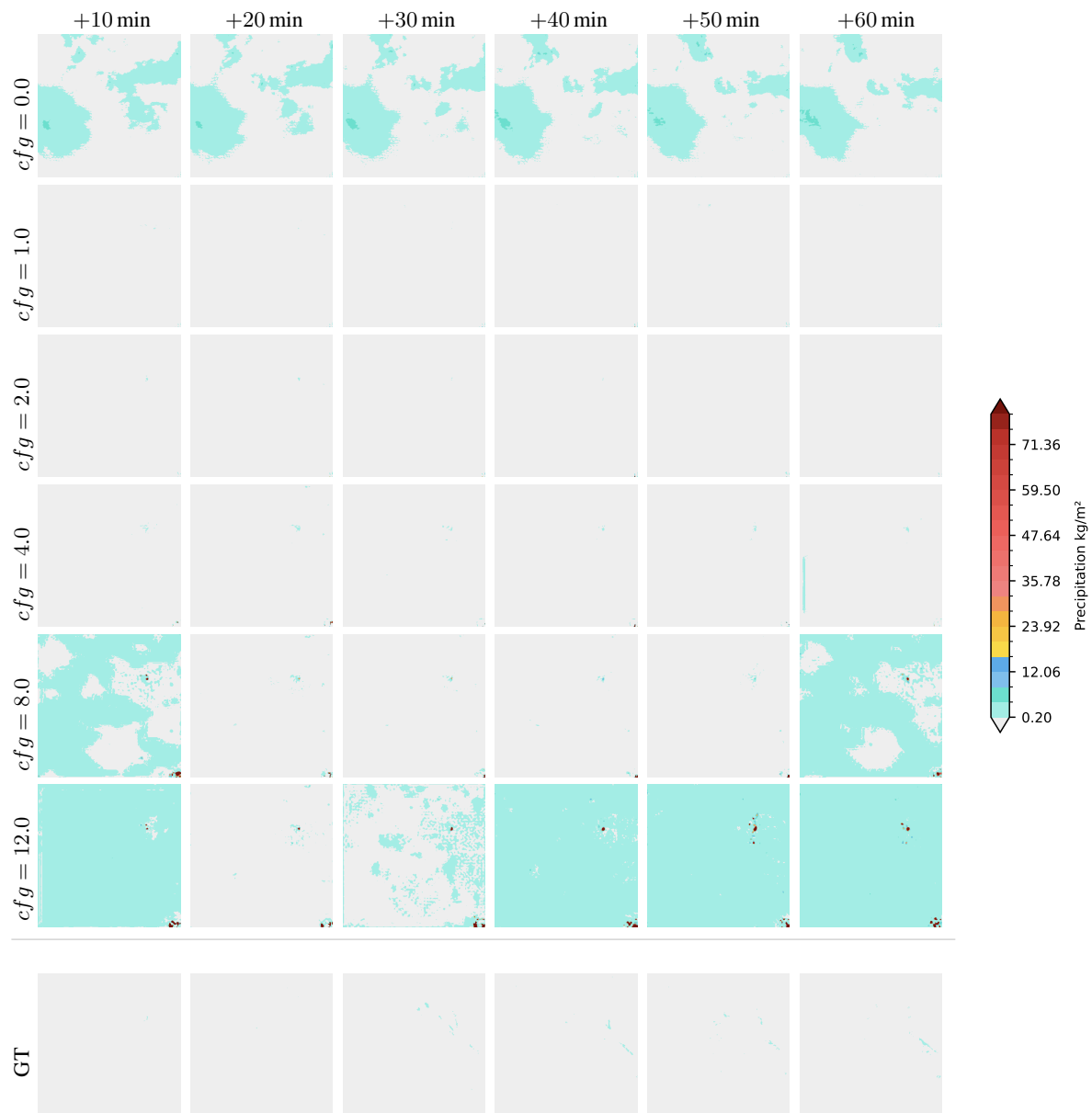


Figure S18. Qualitative results obtained with **CasCast** [40] for different guidance scales [48]. Guidance 0.0 indicates unconditional sampling, while guidance 1.0 indicates conditional sampling without guidance. Best viewed zoomed in.

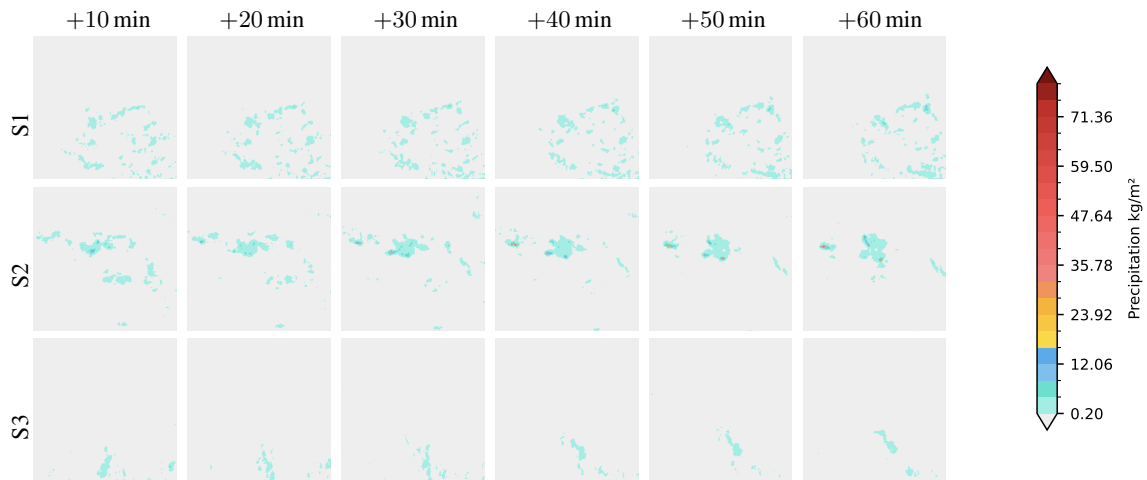


Figure S19. *Unconditional* qualitative samples from the B-LSM in T -reg. latent space. We observe that unconditional samples are temporally consistent, and sharp, but tend to contain low precipitation.

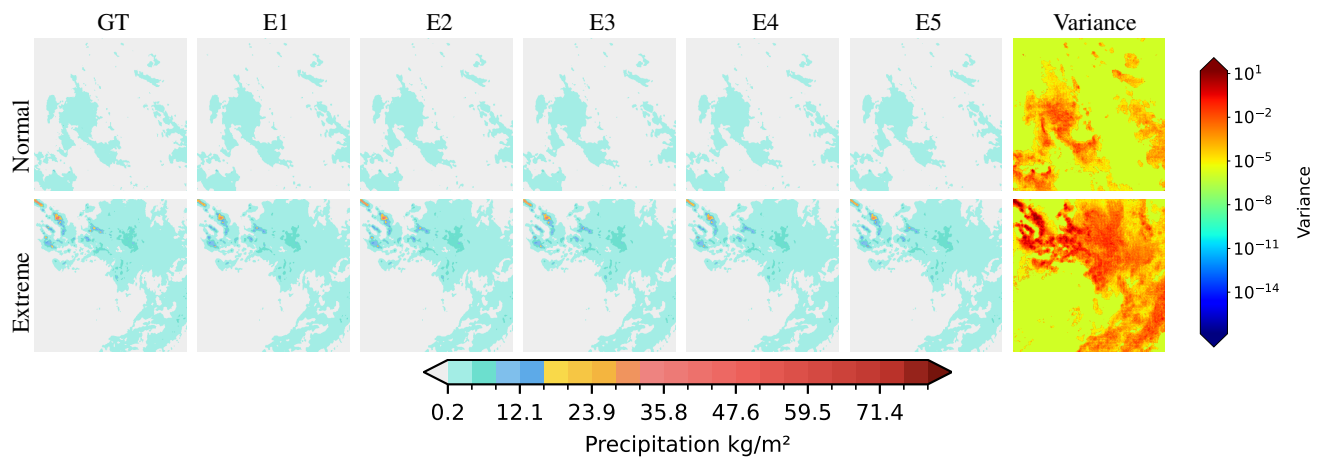


Figure S20. Qualitative reconstruction sampled with the frame-wise DiffAE. Qualitatively, the frame-wise reconstructions match the ground truth well, validating the strong reconstruction performance of the generative decoder.

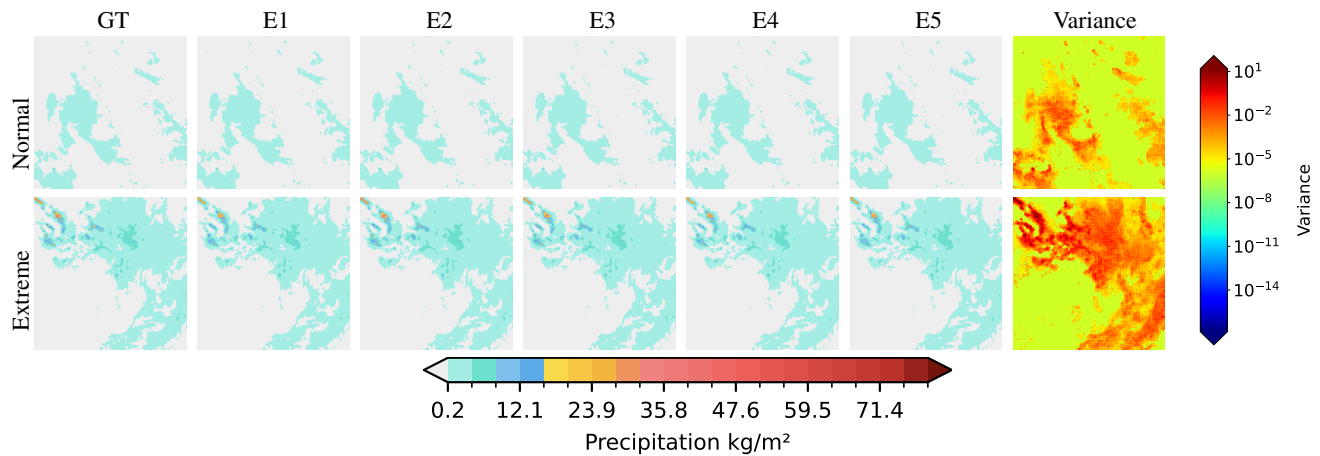


Figure S21. Qualitative reconstruction sampled with the frame-wise DiffAE. Qualitatively, the frame-wise reconstructions match the ground truth well, validating the strong reconstruction performance of the generative decoder.

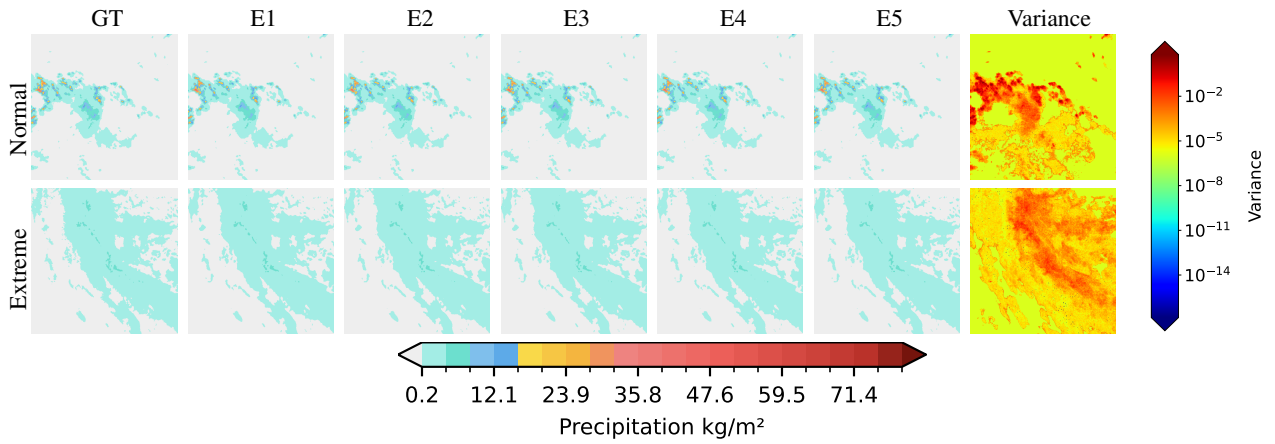


Figure S22. Qualitative results for reconstruction of one normal and one extreme weather event. Variance map uses log scale. Areas with precipitation show higher variance. Areas with extreme precipitation exhibit extreme variance. Best viewed zoomed in.

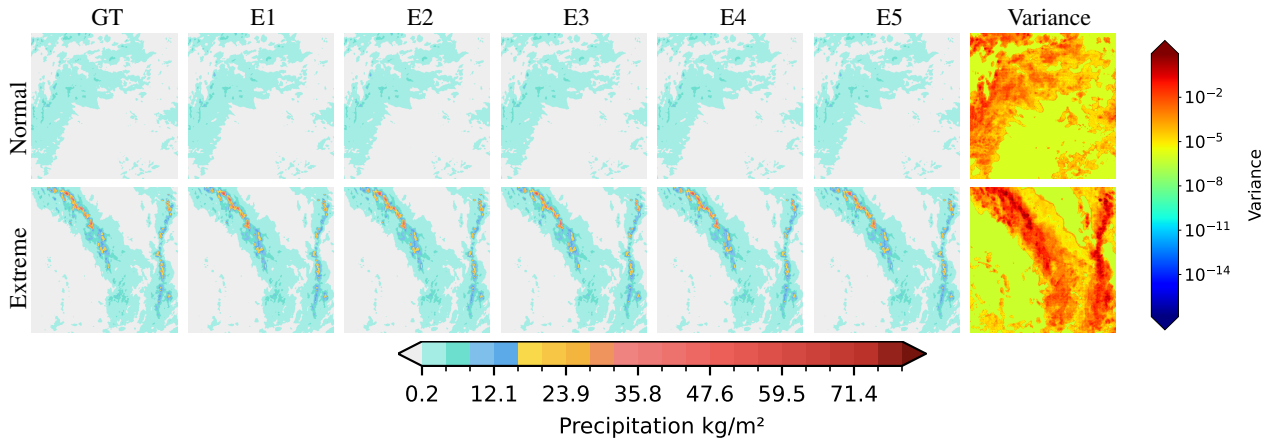


Figure S23. Qualitative results for reconstruction of one normal and one extreme weather event. Variance map uses log scale. Areas with precipitation show higher variance. Areas with extreme precipitation exhibit extreme variance. Best viewed zoomed in.

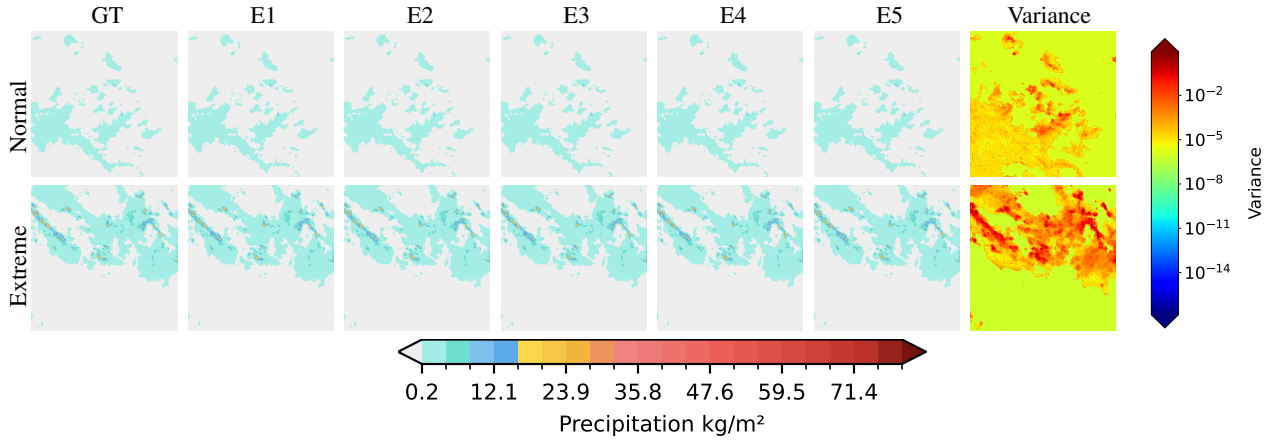


Figure S24. Qualitative results for reconstruction of one normal and one extreme weather event. Variance map uses log scale. Areas with precipitation show higher variance. Areas with extreme precipitation exhibit extreme variance. Best viewed zoomed in.

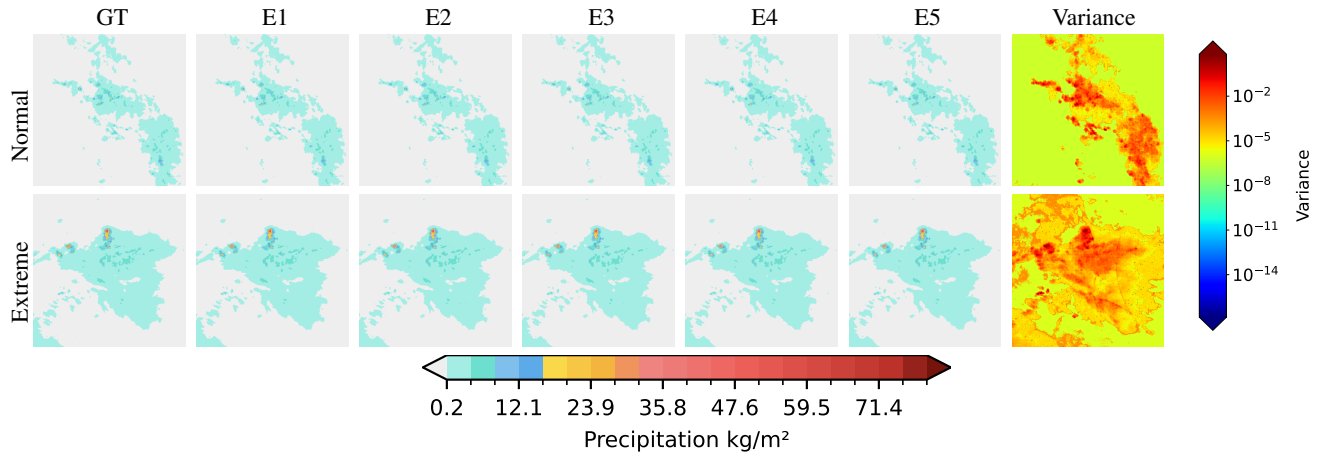


Figure S25. Qualitative results for reconstruction of one normal and one extreme weather event. Variance map uses log scale. Areas with precipitation show higher variance. Areas with extreme precipitation exhibit extreme variance. Best viewed zoomed in.

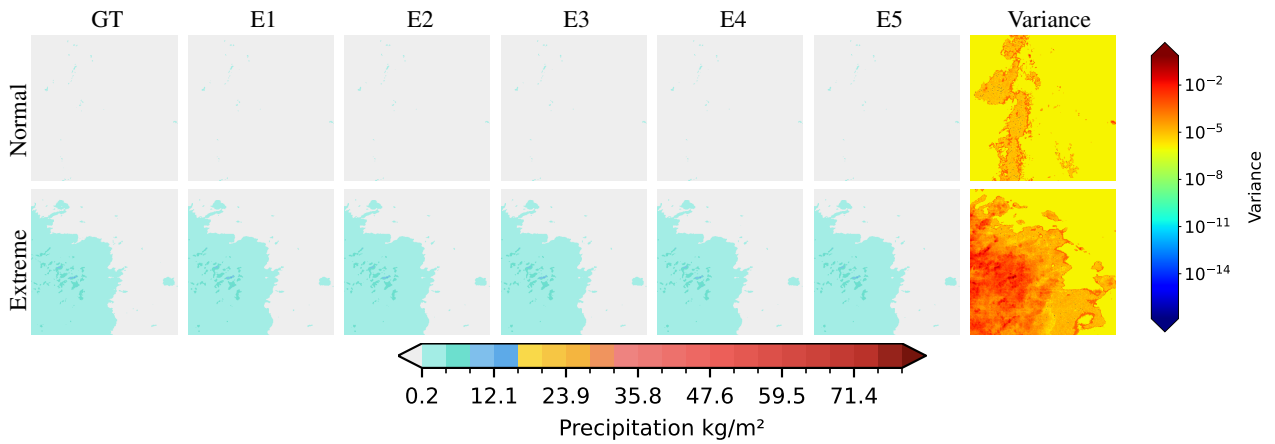


Figure S26. Qualitative results for reconstruction of one normal and one extreme weather event. Variance map uses log scale. Areas with precipitation show higher variance. Areas with extreme precipitation exhibit extreme variance. Best viewed zoomed in.

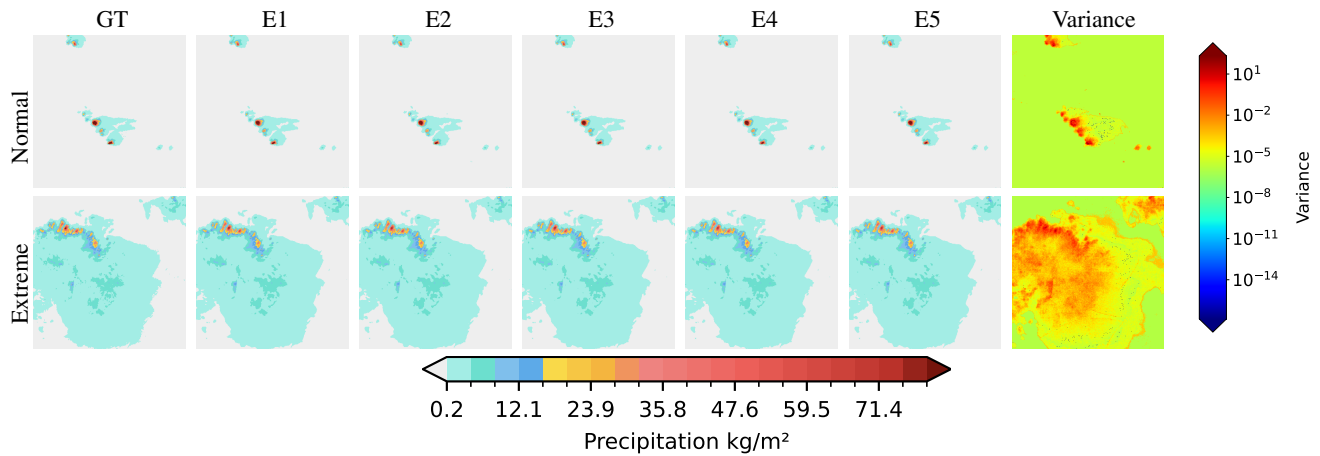


Figure S27. Qualitative results for reconstruction of one normal and one extreme weather event. Variance map uses log scale. Areas with precipitation show higher variance. Areas with extreme precipitation exhibit extreme variance. Best viewed zoomed in.

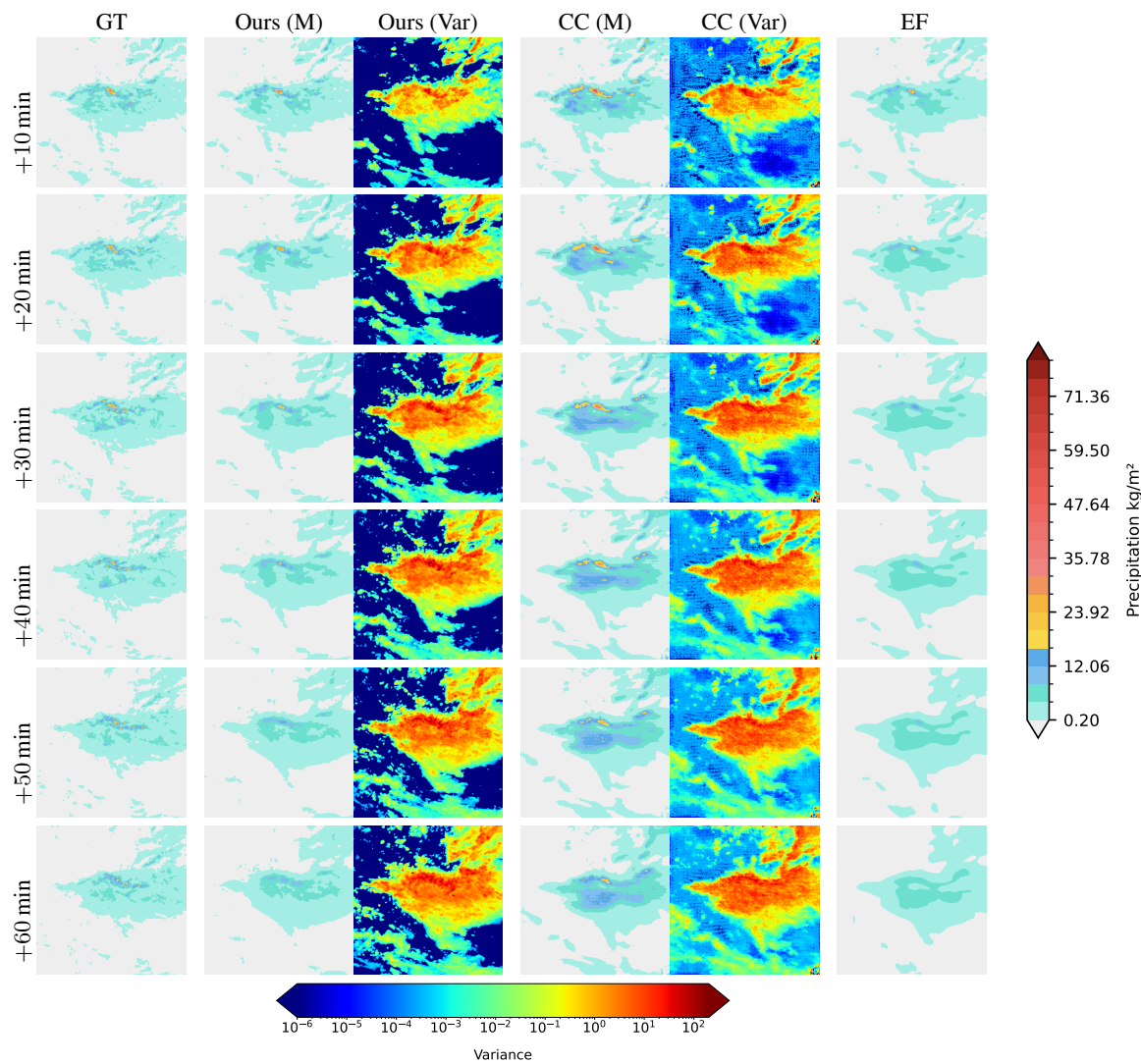


Figure S28. Comparison of forecasts made with our method, CasCast (CC) [40] and Earthformer (EF) [35]. For probabilistic methods, we show the mean (M) forecast and variance (Var) of a 10-member ensemble. Our forecast aligns more closely with the ground truth and variance, while CasCast overestimates and Earthformer underestimates precipitation. Further, the ensemble variance in our method focuses on high precipitation regions in the ground truth. Best viewed zoomed in.

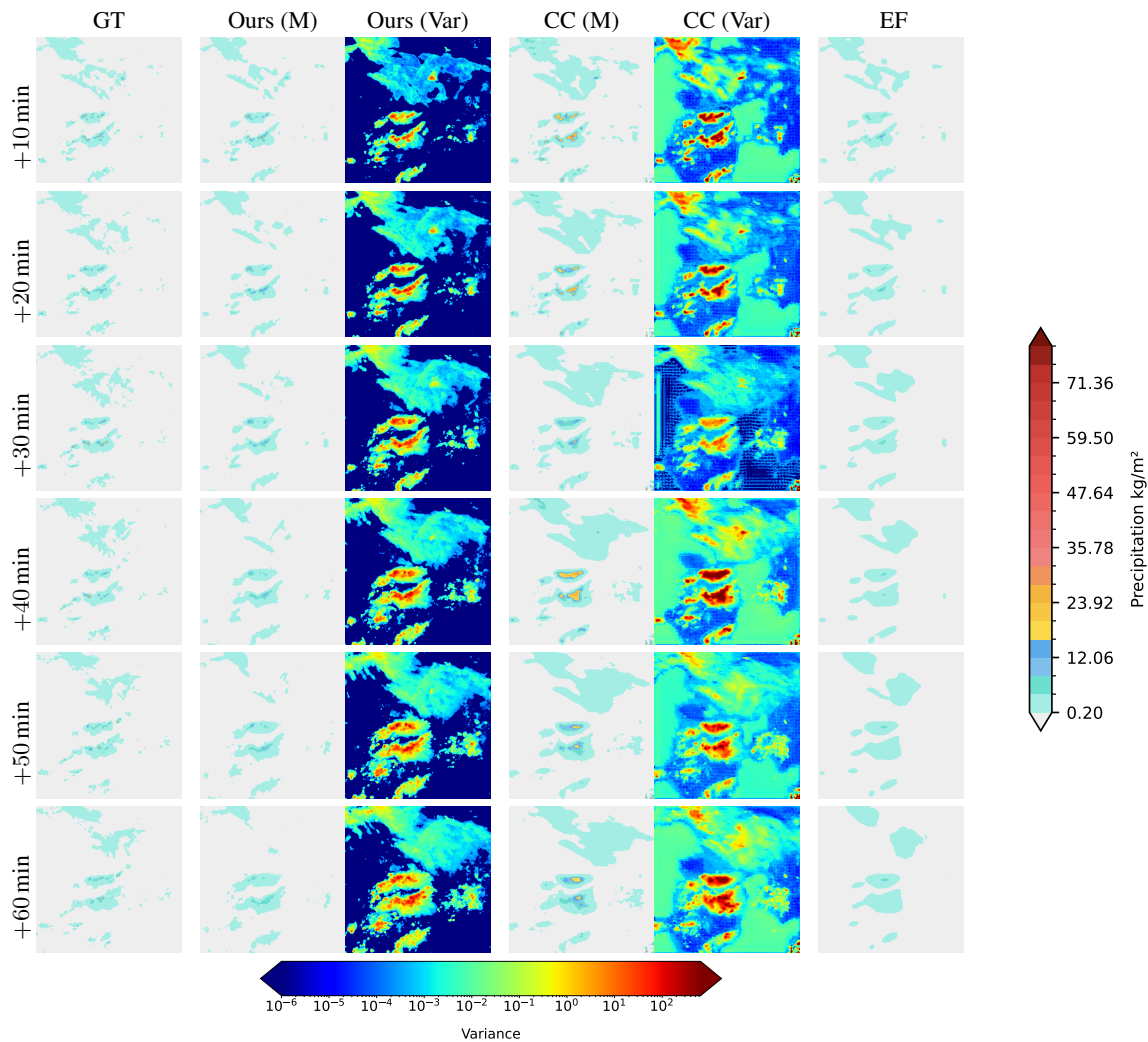


Figure S29. Comparison of forecasts made with our method, CasCast (CC) [40] and Earthformer (EF) [35]. For probabilistic methods, we show the mean (M) forecast and variance (Var) of a 10-member ensemble. Our forecast shows substantially improved temporal consistency compared to CasCast, where a strong precipitation event appears for a single frame. Further, the shape of our forecast aligns more closely with the ground truth. Best viewed zoomed in.

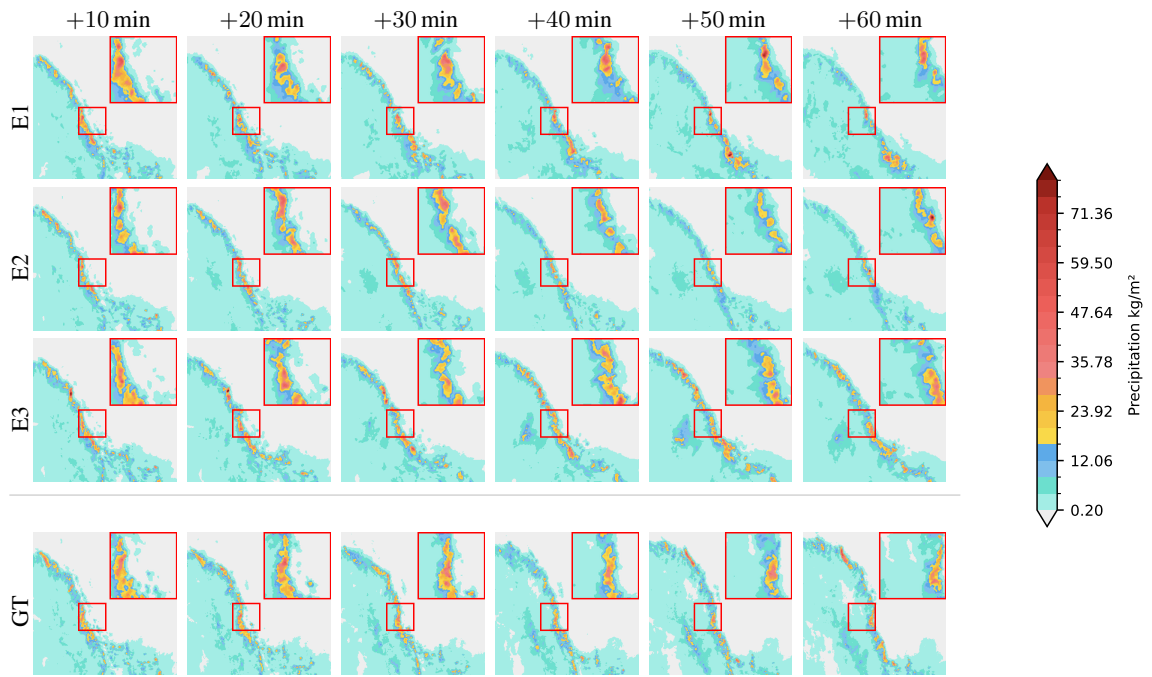


Figure S30. Qualitative result for our L-LSM with *T-reg.* first-stage. The red rectangle highlights a punch-in for better visualization of ensemble differences in details. Best viewed zoomed in.

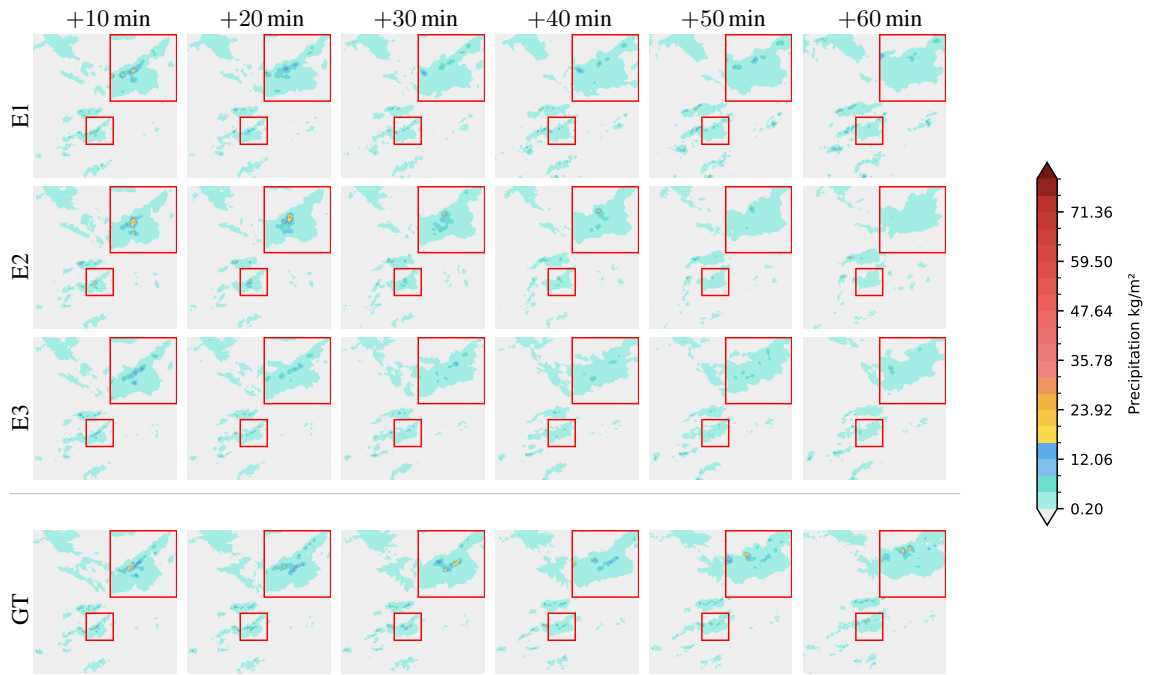


Figure S31. Qualitative result for our L-LSM with *T-reg.* first-stage. The red rectangle highlights a punch-in for better visualization of ensemble differences in details. Best viewed zoomed in.

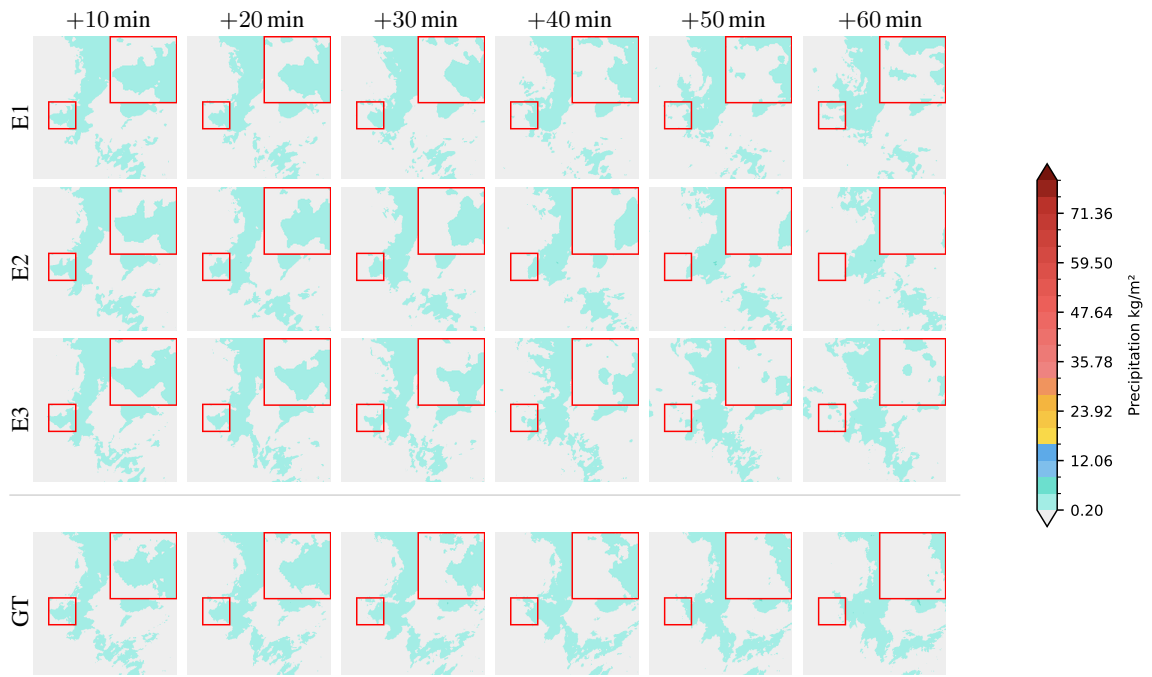


Figure S32. Qualitative result for our L-LSM with *T-reg*. first-stage. The red rectangle highlights a punch-in for better visualization of ensemble differences in details. Best viewed zoomed in.

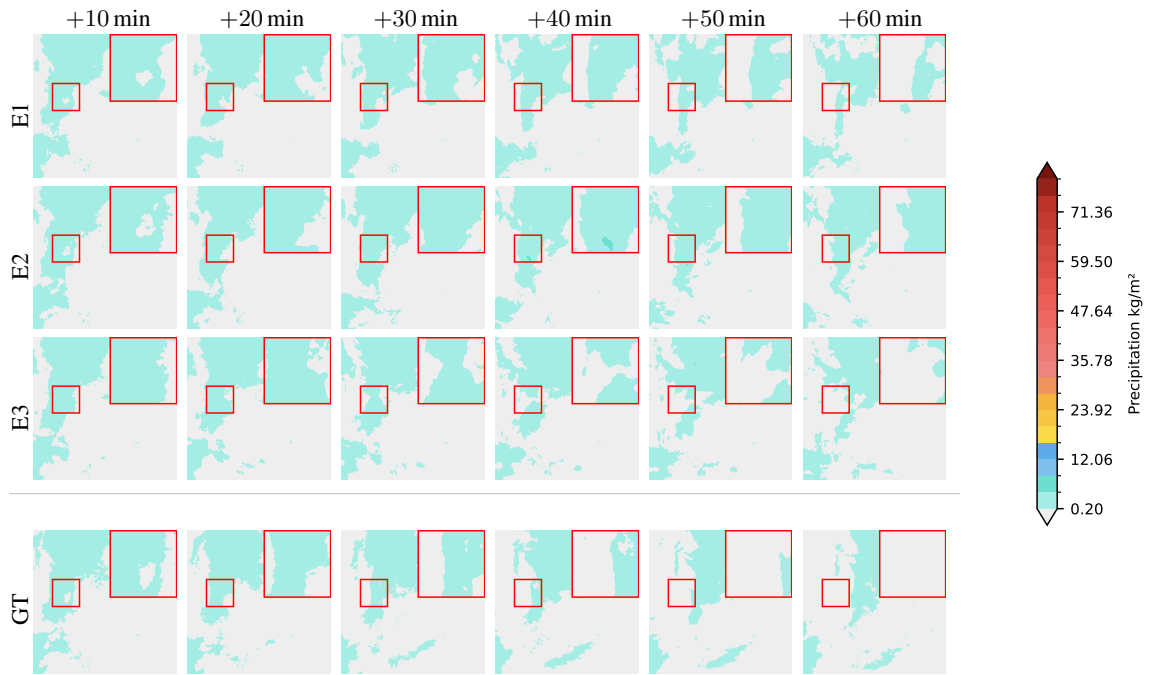


Figure S33. Qualitative result for our L-LSM with *T-reg*. first-stage. The red rectangle highlights a punch-in for better visualization of ensemble differences in details. Best viewed zoomed in.

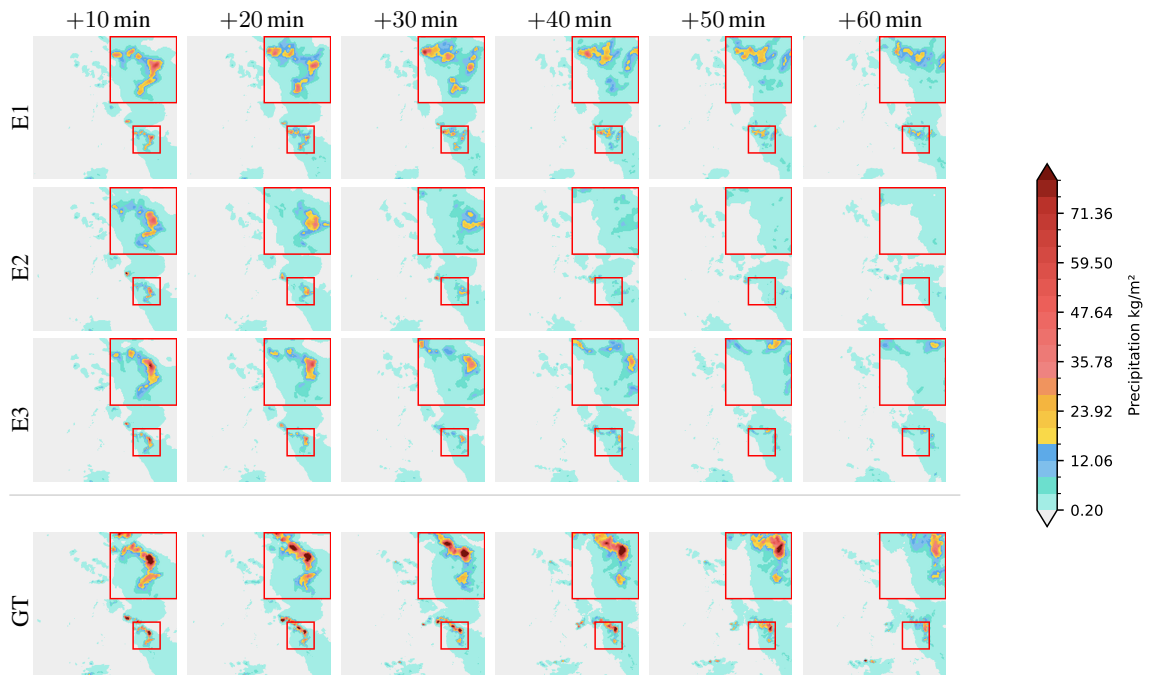


Figure S34. Qualitative result for our L-LSM with $T-reg$. first-stage. The red rectangle highlights a punch-in for better visualization of ensemble differences in details. Best viewed zoomed in.

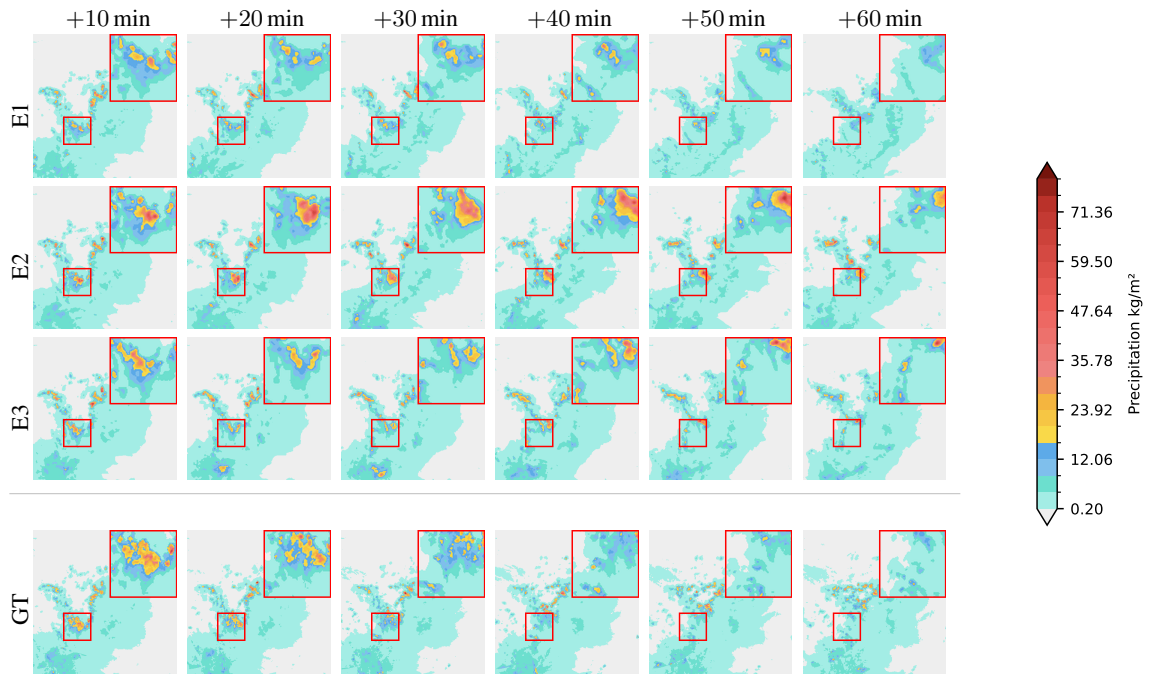


Figure S35. Qualitative result for our L-LSM with $T-reg$. first-stage. The red rectangle highlights a punch-in for better visualization of ensemble differences in details. Best viewed zoomed in.

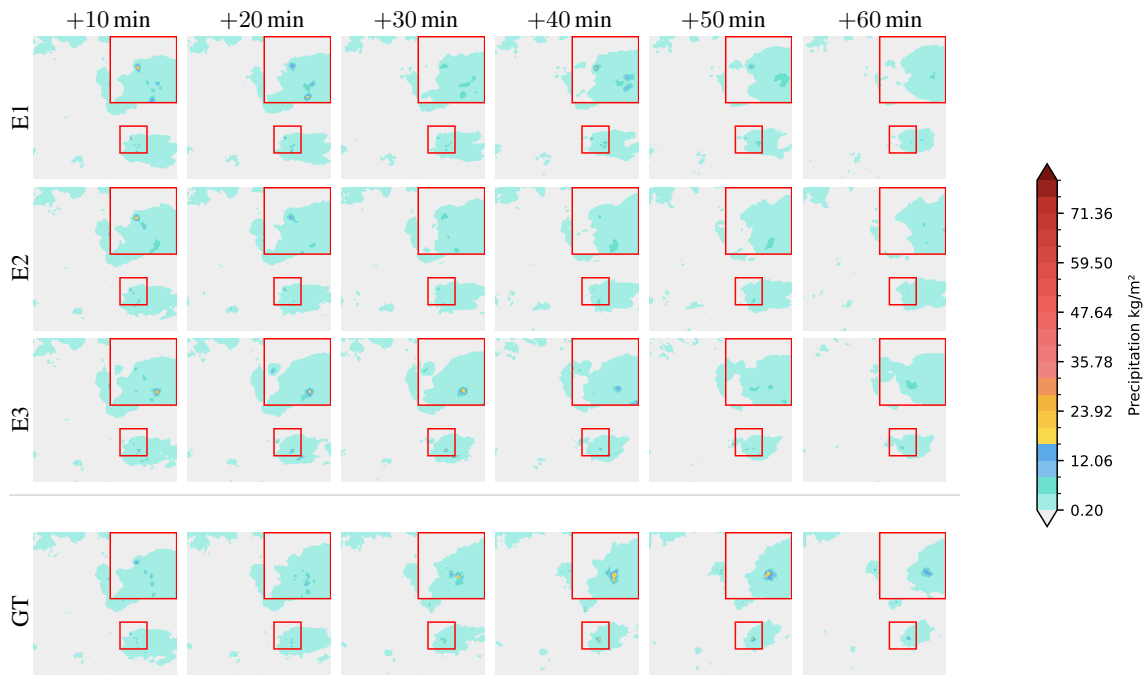


Figure S36. Qualitative result for our L-LSM with *T-reg.* first-stage. The red rectangle highlights a punch-in for better visualization of ensemble differences in details. Best viewed zoomed in.

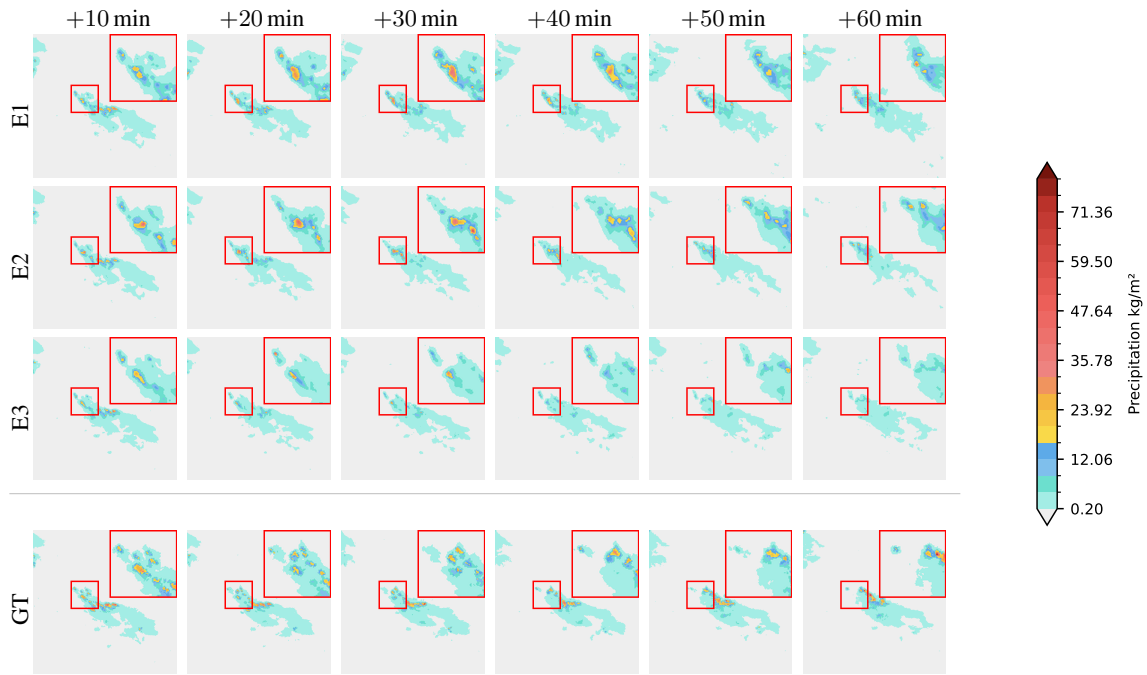


Figure S37. Qualitative result for our L-LSM with *T-reg.* first-stage. The red rectangle highlights a punch-in for better visualization of ensemble differences in details. Best viewed zoomed in.